




Optimizing the Performance of Aerosol Photoacoustic Cells using a Finite Element Model. Part 2: Application to a Two-Resonator Cell

Michael I. Cotterell, Gareth P. Ward, Alastair P. Hibbins, Andy Wilson, Jim M. Haywood & Justin M. Langridge

To cite this article: Michael I. Cotterell, Gareth P. Ward, Alastair P. Hibbins, Andy Wilson, Jim M. Haywood & Justin M. Langridge (2019): Optimizing the Performance of Aerosol Photoacoustic Cells using a Finite Element Model. Part 2: Application to a Two-Resonator Cell, Aerosol Science and Technology, DOI: [10.1080/02786826.2019.1648749](https://doi.org/10.1080/02786826.2019.1648749)

To link to this article: <https://doi.org/10.1080/02786826.2019.1648749>

 View supplementary material [↗](#)

 Accepted author version posted online: 31 Jul 2019.

 Submit your article to this journal [↗](#)

 Article views: 33

 View related articles [↗](#)

 View Crossmark data [↗](#)

Optimizing the Performance of Aerosol Photoacoustic Cells using a Finite Element Model. Part 2: Application to a Two-Resonator Cell

Michael I. Cotterell^{1,2}, Gareth P. Ward³, Alastair P. Hibbins³, Andy Wilson², Jim M. Haywood^{1,2} and Justin M. Langridge²

¹College for Engineering, Mathematics and Physical Sciences, University of Exeter, Exeter, United Kingdom

²Observation Based Research, Met Office, Exeter, United Kingdom

³Electromagnetic and Acoustic Materials Group, Department of Physics and Astronomy, University of Exeter, Exeter, United Kingdom

CONTACT Michael I. Cotterell m.cotterell@exeter.ac.uk College for Engineering, Mathematics and Physical Sciences, University of Exeter, Laver Building, North Park Road, Exeter, EX4 4QF, UK.

EDITOR:

Abstract

Photoacoustic spectroscopy (PAS) measures aerosol absorption in a non-contact manner, providing accurate absorption measurements that are needed to improve aerosol optical property representations in climate models. Central to PAS is resonant amplification of the acoustic pressure wave generated from laser-heated aerosol transferring heat to surrounding gas by a photoacoustic cell. Although this cell amplifies pressure sources from aerosol absorption (*signal*), it also amplifies noise and *background* sources. It is important to maximise the cell signal-to-background ratio (SBR) for sensitive absorption measurements. Many researchers have adopted the two-resonator cell design described by Lack *et al.* (2006). We show that the uncertainty in PAS measurements of aerosol absorption using this two-resonator cell is significantly degraded by its large sensitivity to background contributions from laser scattering and absorption at the cell windows. In Part 1, we described the use of a finite element method (FEM) to predict cell acoustic properties, validated this framework by comparing model predictions to measurements, and used FEM to test various strategies applied commonly to single-resonator cell optimisation. In this second part, we apply FEM to understand the excitation of resonant modes of the two-resonator cell, with comparison measurements demonstrating accurate predictions of acoustic response. We perform geometry optimisation studies to maximise the SBR and demonstrate that the laser-window interaction background is reduced to undetectable levels for an optimal cell. This optimised two-resonator cell will improve the sensitivity and accuracy of future aerosol absorption measurements.

1. Introduction

The scattering and absorption of light by aerosol particles are important processes occurring in our atmosphere. Indeed, the magnitudes of aerosol-light interactions remain one of the largest uncertainties in climate models (Alexander *et al.* 2013), with the radiative impact from light absorbing aerosol constrained poorly in particular (Stier *et al.* 2007). Large uncertainties in absorption arise from a lack of accurate absorption measurements for atmospheric aerosol and how absorption evolves over particle lifetime and with atmospheric processing (Wang *et al.* 2018; Laskin *et al.* 2015; Moise *et al.* 2015). Reducing these uncertainties requires

improved instrumentation for accurate and sensitive measurements of aerosol light absorption coefficients (α_{abs}) (Moosmüller et al. 2009).

Traditionally, α_{abs} have been derived from the transmission of light through a filter onto which aerosol is collected, but large uncertainties (of up to 80%) are associated with the derived values of α_{abs} (Lack et al. 2008, 2009; Cappa et al. 2008), although recent advanced correction schemes show modest biases in derived α_{abs} values of up to 17% (Davies et al. 2019). These uncertainties arise mostly from the modification of aerosol microphysical properties through interactions with a filter substrate. In recent years, researchers have made significant developments of non-contact techniques for α_{abs} measurements. Such measurement approaches have included calculation of α_{abs} from the difference in measured scattering (α_{sca}) and extinction ($\alpha_{ext} = \alpha_{sca} + \alpha_{abs}$) coefficients using nephelometry and cavity ring-down spectroscopy respectively (Strawa et al. 2003). However, this ‘difference’ approach often leads to significant uncertainties in α_{abs} when α_{abs} is small. As discussed by Sedlacek and Lee (2007), applying the difference method when α_{abs} is small involves the subtraction of two quantities with similar magnitudes, with the standard error in the extinction and scattering measurements combining to give significant uncertainty (>60%) in the derived α_{abs} . Thus, non-contact techniques that probe absorption *directly* are required. Both photothermal interferometry (Sedlacek and Lee 2007; Sedlacek 2006) and – the focus of this work – photoacoustic spectroscopy (PAS) measure α_{abs} directly for aerosol in its natural suspended state. These approaches are the techniques-of-choice for accurate, direct and non-contact measurements of aerosol α_{abs} .

A full description of PAS is provided in Sect. 2. Briefly, the consequent periodic pressure wave generated by continuous cycles of laser-induced aerosol heating is measured. This periodic pressure wave results from particles liberating their heat to the bath gas through collisional quenching and the gas undergoing adiabatic cycles of thermal expansion/contraction at a frequency commensurate with the laser modulation frequency. A photoacoustic cell (PA cell) resonantly amplifies the pressure wave for detection by a sensitive microphone, with the amplitude of the microphone response directly proportional to the aerosol absorption coefficient. PAS has been used in laboratory studies to measure α_{abs} for soot particles (Linke et al. 2016; Yelverton et al. 2014; Sharma et al. 2013; Ajtai et al. 2010) and so-called brown carbon particles produced from the oxidation of toluene organic aerosol in the presence of NO_x (Nakayama et al. 2010). Meanwhile, field studies have included ground based measurements (Bluvshtein et al. 2016; Cappa et al. 2008) and measurements from aircraft platforms (Peers et al. 2019; Davies et al. 2019; Lack et al. 2012; Arnott et al. 2006). Our research uses a suite of photoacoustic and cavity ring-down spectrometers to measure absorption and extinction coefficients for laboratory generated aerosol or atmospheric aerosol from aboard research aircraft platforms. By comparing PAS measurements of absorption with that expected from Mie theory, our laboratory measurements (Davies et al. 2018) have demonstrated that PAS measures α_{abs} to an accuracy better than 8% at optical wavelengths of 405, 514 and 658 nm, i.e. discrete wavelengths that span the visible spectrum. Moreover, Table S1 of Fischer and Smith (2018) shows that PAS measurements of aerosol absorption often achieve sensitivities <1 Mm⁻¹.

A key consideration of any photoacoustic instrument is the design of the PA cell for the amplification of the periodic photoacoustic pressure wave. The cell is a resonance chamber, where induced pressure waves couple to the resonant mode of the cell when the frequencies are matched. A typical PA cell consists of one or two cylindrical resonators capped by acoustic buffer volumes. While many studies have used single-resonator cells of various sizes (Yu et al. 2017; Linke et al. 2016; Nakayama et al. 2015; Radney and Zangmeister 2015), recent field and laboratory measurements by a growing number of research groups (Peers et

al. 2019; Foster et al. 2019; Davies et al. 2019; Cotterell et al. 2019a; Fischer and Smith 2018a, 2018b; Davies et al. 2018; Bluvshstein et al. 2017; Zhang et al. 2016; Lack et al. 2012) have used a two-resonator cell with the same geometry as described in Lack et al. (2006). This two-resonator cell contains a microphone in each resonator, with the microphone signals passed to a differential amplifier to subtract in-phase components of the signals. The uncertainties in PAS measurements of α_{abs} for spectrometers using this two-resonator cell were assessed by Lack et al. (2012) from both laboratory and aircraft-based studies. The sensitivity in α_{abs} was determined to lie in the range $0.5 - 1.5 \text{ Mm}^{-1}$, with an accuracy of $\sim 10\%$ for α_{abs} measurements performed from an aircraft platform. Similarly, we have performed our own uncertainty analysis for PAS-measured α_{abs} (using the two-resonator cell design of Lack *et al.*) during measurements aboard the UK research aircraft (FAAM BAe-146). Figure 1(a) shows typical flight data, showing the variation in raw microphone response during a series of straight and level aircraft runs performed at altitudes in the pressure range $550 - 1000 \text{ hPa}$. The large observed microphone response at pressures above 650 hPa were associated with the aircraft entering an aerosol layer. The plot also shows measurements of the background microphone response at discrete moments in time when filtered air, devoid of any light absorbing sample, was drawn through the PA cell. There is always a significant background contribution to the raw microphone response. Moreover, this background depends strongly on pressure; the background microphone response is lower at reduced pressure. This background arises almost entirely from the laser beam interacting with the PA cell windows through light scattering (where photon momentum is transferred to the window surface causing mechanical vibrations) and absorption (with light heating the window and generating an additional photoacoustic source). In processing the raw microphone data to calculate α_{abs} , the background is subtracted. Because the background response cannot be measured at all times, the data analysis relies on a pressure-dependent interpolation to achieve this background subtraction. Figure 1(a) shows this interpolated background, using the fit of a quadratic polynomial to the measured pressure variation in the background. Uncertainty in the background interpolation degrades the accuracy in the derived aerosol absorption; Figure 1(b) shows the percentage error in α_{abs} associated with the uncertainty in the background interpolation with variation in the aerosol absorption amplitude. The standard error in α_{abs} can be as high as $10 - 20\%$ for α_{abs} in the range $1 - 5 \text{ Mm}^{-1}$, i.e. for typical levels of aerosol absorption. Clearly, removing the dominant background associated with laser-window interactions would considerably reduce the uncertainty and improve the sensitivity in α_{abs} measurements using the two-resonator cell. Therefore, the cell should amplify the aerosol absorption response (signal) and suppress, or indeed remove, the detection of laser-window interactions (background); any cell optimisation study should aim to maximise the *signal-to-background ratio* (SBR).

The design for the current two-resonator cell design was not based on acoustic modelling. Instead, Lack et al. (2006) were inspired by the cell design of Krämer et al. (2001), using two resonators that each contained a microphone. A differential amplifier subtracted the two microphone signals and the authors envisaged that in-phase noise would be removed from the measured response. As shown above, this differential operation does not remove the window background in the Lack *et al.* cell design; as we will demonstrate, the response in the two resonators are coupled strongly. Importantly, no study has attempted to optimise the two-resonator cell, despite its widespread adoption by other research groups. In the companion paper (Part 1), we described a Finite Element Method (FEM) framework for predicting the acoustic performance of PA cells. We then validated this framework by comparing model predictions of acoustic properties to measurements for a single-resonator multipass PA cell, the generic structure often used in aerosol cells. We then used this model framework to assess the effectiveness of a range of strategies applied commonly to the optimisation of photoacoustic sensitivity for single-resonator cells. In this second part, we apply FEM to the

analysis of the two-resonator cell that has recently gained widespread use in leading aerosol absorption measurement research, and optimise its performance to completely suppress the detection of laser-window interactions. Section 2 describes the principles of photoacoustic spectroscopy and the resonant excitation of PA cell modes. Section 3 describes the FEM model used to describe sample and window heating for our two-resonator cell, and describes our measurement cells that were used in validating our model predictions. Section 4 presents an analysis of the acoustic behaviour of the existing two-resonator cell before performing optimisation studies to design a cell that is insensitive to laser-window interactions.

2. Principles of photoacoustic spectroscopy

The PA process has been described in detail by Rosencwaig (1980), Miklós et al. (2001) and in our companion paper (Cotterell et al. 2019b). Intensity modulated laser light is absorbed by a sample through excitation of molecular rotational, vibrational and/or electronic energy levels. If the fate of excited molecules is dominated by collisional relaxation (and radiative relaxation, photo-dissociation and latent heat energy pathways can be ignored), energy is transferred to translational degrees of freedom of the bath gas. This heat transfer causes thermal expansion and generates a pressure wave; the magnitude of this pressure wave is proportional to α_{abs} . Central to the PA process is the amplification of the pressure wave through excitation of an acoustic eigenmode (standing wave) associated with the geometry of the PA cell. In resonant PAS, the laser power is modulated periodically at the resonance frequency (eigenfrequency) corresponding to the cell eigenmode. Repeated cycles of bath gas thermal expansion/contraction generate a periodic pressure wave that couples efficiently into the cell eigenmode, providing there is sufficient spatial overlap of the eigenmode pressure $p_n(\vec{r})$ and the heat deposition $H(\vec{r})$ distributions (see below). The eigenmode has an associated quality factor (Q) describing the energy stored in the resonator relative to the energy lost over one complete period. Typically, Q is greater than 50 (Davies et al. 2018; Lack et al. 2012), amplifying the amplitude of the photoacoustic pressure wave by the same factor for subsequent detection by a sensitive microphone located within the cell. Typically, the detected pressure response is on the order of ~ 10 μ Pa and is linearly proportional to α_{abs} (Lack et al. 2006, 2012; Bijnen et al. 1996). By calibrating the PAS with a species of known absorption (typically a gaseous absorber, the absorption for which is verified using an independent calibration-free technique such as cavity ring-down spectroscopy), α_{abs} is determined from the microphone response.

To understand the excitation of modes of an acoustic cavity (i.e. our PA cell), it is useful to consider the general solution to the time-independent wave equation. In the limit of adiabatic compression/expansion during acoustic compression/expansion cycles for an ideal gas, the acoustic pressure distribution $p(\vec{r})$ is found by solving the inhomogeneous wave equation. We write the general solution to this equation as a sum of excitations of resonant eigenmodes $p_n(\vec{r})$ of the cell. These eigenmodes are orthogonal and have associated resonance frequencies f_n . Thus, we write the frequency-dependence in the pressure at the microphone location $p(\vec{r}_M, \omega)$ as a sum over eigenmode excitations:

$$p(\vec{r}_M, \omega) = \sum_n \frac{i\omega(\sigma-1)I_0}{(\omega_n^2 - \omega^2 + i\frac{\omega\omega_n}{Q_n})} \frac{\int g(\vec{r})\alpha_{abs}(\vec{r})p_n(\vec{r})dV}{V} p_n(\vec{r}_M) \quad 1$$

in which $p_n(\vec{r}_M)$ is the eigenmode pressure at the microphone position, ω is the angular frequency of the periodically modulated heat (laser intensity) source, ω_n is the resonance angular frequency ($\omega_n = 2\pi f_n$) and Q_n is the quality factor associated with energy losses through thermal and viscous damping processes. A low Q_n corresponds to high levels of thermal and viscous damping. Other important terms are the adiabatic coefficient (σ), the

laser intensity amplitude (I_0), the laser intensity spatial distribution ($g(\vec{r})$, e.g. a Gaussian), and the cell volume (V).

The microphone response is given by the absolute value of $p(\vec{r}_M)$ which, for the efficient excitation of a single eigenmode, is given by:

$$|p(\vec{r}_M, \omega)| = (\sigma - 1)I_0 p_n(\vec{r}_M) \frac{J_n}{V} \sqrt{\frac{Q_n^2/\omega_n^2}{1+Q_n^2(\frac{\omega_n-\omega}{\omega})^2}} \quad 2$$

Here, we have defined the overlap integral $J_n = \int g(\vec{r})\alpha_{abs}(\vec{r})p_n(\vec{r})dV$. This overlap integral for the spatial distributions in the laser power, light absorbing sample and pressure eigenmode impacts strongly on the excitation amplitude of a cell resonance. We can assume the absorbing sample occupies the cell homogeneously and the overlap integral is written as $J_n = \alpha_{abs} \int g(\vec{r})p_n(\vec{r})dV$. Thus, we can describe the frequency-dependent microphone response as a function of the form:

$$|p(\vec{r}_M, \omega)| = p_0 \sqrt{\frac{1}{1+Q_n^2(\frac{\omega_n-\omega}{\omega})^2}} \quad 3$$

The general expressions of equations 1 and 2 are useful in describing the manifestation of resonant mode excitation, the functional form of the frequency-dependent microphone response and the role of the overlap integral in determining mode excitation amplitudes. However, we require quantitative calculations of eigenmode pressure distributions $p_n(\vec{r})$ to predict the microphone response for a given cell geometry. This requires numerical methods such as FEM.

3. Experimental and numerical methods

3.1. A finite element model to predict the acoustic behaviour of a two-resonator PA cell

We used FEM to predict the eigenmode pressure distributions $p_n(\vec{r})$ and frequency-dependent microphone response $|p(\vec{r}_M, \omega)|$ for our two-resonator PA cell and optimise the cell geometry to maximise the SBR. This section provides a brief overview of FEM for predicting PA cell acoustic properties before describing the specific model used to represent our two-resonator cell; the reader is directed to our companion publication for complete details of the principles of using FEM to predict photoacoustic phenomena (Cotterell et al. 2019b).

The amplification of ~kilohertz frequency acoustic waves by a photoacoustic cell is a thermo-viscous acoustic process. We are required to solve a set of four equations to predict thermo-viscous acoustic phenomena that involve the perturbations of the three properties of pressure, temperature and velocity. This set of equations include the momentum equation, continuity equation, Fourier heat law and an equation of state. Forming an analytical solution that satisfies these equations is not possible for most geometries and instead we use numerical methods to solve the pressure, temperature and velocity fields. In FEM, we divide our geometry into many small elements using a *mesh* of tetrahedral elements. The thermo-viscous acoustic equations are solved numerically for each mesh element, with the solutions for adjacent elements coupled by boundary conditions. Importantly, the internal surfaces of the PA cell contribute to damping of acoustic energy through thermal and viscous damping. Thermal damping arises from the isothermal heat transfer between the high thermal conductivity surfaces of typical metal cells and the closest layer of air. Viscous damping arises from the no-slip boundary condition that requires the tangential velocity be zero for

molecules closest to the cell surfaces. As we show in our companion paper for a 1500 Hz acoustic wave in air, thermal and viscous energy losses occur over boundary layer thicknesses of $\sim 70 \mu\text{m}$ and $\sim 60 \mu\text{m}$, respectively (Cotterell et al. 2019b). These thermal and viscous boundary layer losses are the dominant contributors to damping and thus lead to the reduction of Q factors for resonant modes.

To calculate eigenmode pressure distributions and frequency-dependent microphone responses, we used the thermoviscous acoustics interface in the FEM modelling software COMSOL Multiphysics 5.2a. We investigated the performance of our two-resonator cell for the cases of using either flat or Brewster angled windows. While our measurements have exploited Brewster-angled windows to minimise scattering of incident laser light (Cotterell et al. 2019a; Davies et al. 2018), researchers using the same cell design have used flat windows (Foster et al. 2019; Fischer and Smith 2018b; Bluvshstein et al. 2017; Lack et al. 2012). Figure 2(a) and (b) show the respective meshed geometries for the flat and Brewster-angled window cells; the Brewster window cell mimics the flat window cell, albeit having additional Brewster-angled volumes. Moreover, Figure 2(c) labels the parameters that describe completely the cell geometries and Table 1 provides values for these parameters that describe the cells used in our own measurements and in studies by other researchers. The cells consist of two parallel and cylindrical resonators (an *upper* and *lower* resonator), each of length l_{res} and radius r_{res} , that are separated by a centre-to-centre distance d_{res} and connected by capping buffer volumes affixed to each resonator end. These buffer volumes are characterised by a length l_{buf} , height h_{buf} , width w_{buf} and a fillet radius r_{fil} . Each buffer volume is affixed to a cylindrical volume (referred to as *window volumes*) onto which windows are affixed. The window volumes have a length l_{win} and radius r_{win} . We applied two mirror symmetry boundaries to reduce computational cost, with these two mirror planes indicated in Figure 2(a). Specifically, there is mirror symmetry in the z - x plane (*longitudinal* mirror plane) and in the z - y plane (*transverse* mirror plane). All domains are solved for in the COMSOL Multiphysics thermoacoustics frequency domain interface with equilibrium temperature and pressure set to $T_0 = 293.15 \text{ K}$ and $p_0 = 101325 \text{ Pa}$ (one atmosphere). All the required thermodynamic properties of air (e.g. viscosity, equilibrium density, heat capacity and thermal conductivity) are taken from the COMSOL Multiphysics material library. We assigned no-slip and isothermal boundary conditions to all surfaces of the cell.

An important consideration in any FEM model is the division of the geometry into mesh elements; FEM calculations are computationally expensive if the mesh is very fine, while a coarse mesh will fail to capture important physical processes. Figure 2(a) and (b) show the PA cell models including the finite element mesh. The mesh consisted of a bulk and boundary layer mesh, with the latter mesh of a higher spatial resolution to resolve thermal and viscous damping at the air-surface interface. The bulk mesh had a maximum and minimum tetrahedral element size of 5.72 mm (corresponding to $\sim 1/40$ of the acoustic wavelength) and 1.15 mm ($\sim 1/200$ of the acoustic wavelength), respectively. Other relevant bulk mesh parameters include the maximum element growth rate, curvature factor and resolution of narrow regions, which were set to 1.5, 0.3 and 0.7 respectively. For the boundary layer mesh, the maximum layer decrement was set to 300, with 10 layers resolving a total boundary layer mesh thickness of $100.6 \mu\text{m}$. Our model ignores some aspects of our measurement cell that would prevent mirror symmetry planes being used and lead to long calculation times, including a humidity probe that is inserted into the cell during measurements, small electret microphones located at each resonator centre, a miniature speaker that is located within the lower resonator, and the sample inlet/outlet ports.

In our experimental measurements, a multi-pass laser beam propagates parallel to the x -axis through the centre of the lower resonator. Figure 2(d) shows the domains that were heated in

our Brewster-angled window cell model to represent sample heating. The heat deposited H was represented by:

$$H(\vec{r}) = I_0 g(\vec{r}) = \frac{I_0}{\pi w^2} \exp\left(-\frac{y^2+z^2}{2w^2}\right) \alpha_{abs} \quad 4$$

with the laser intensity spatial distribution $g(\vec{r})$ described by a Gaussian distribution of beam waist w , while y and z represent the transverse distances from the cylindrical axis through the centre of the lower resonator. In all simulations of sample heating, we used $I_0 = 0.1$ W, $w = 0.5$ mm and a sample absorption coefficient $\alpha_{abs} = 5$ Mm⁻¹, a typical absorption coefficient for atmospheric aerosol (Lack et al. 2012). The important parameter for geometry optimisation is the SBR, requiring simulations of microphone responses for both sample heating and laser-window interactions. Figure 2(d) shows the window-heating domain used in simulating the latter microphone responses in the Brewster cell, with the cylindrical heating domain oriented at the Brewster angle, having a radius $0.9r_{win}$, thickness 2 mm, and located 1 mm from the boundary of the window volume. The window-heating domain for the flat-window cell took similar dimensions, but was oriented such that the incident laser beam propagated normal to the window face. The heat deposited in the window-heating domain was also described by equation 4 using the same parameters above, albeit using the absorption coefficient for N-BK7 glass (<https://refractiveindex.info/>) at a 550 nm optical wavelengths ($\alpha_{abs} = 0.1653$ m⁻¹). We did not include any pressure sources to mimic light scattering from the cell windows as this proved not possible in the COMSOL Multiphysics thermos-viscous acoustics interface without perturbing the no-slip and isothermal boundary conditions.

COMSOL Multiphysics was used to simulate the eigenmode pressure distributions $p_n(\vec{r})$ and their associated eigenfrequencies. Furthermore, we modelled the frequency-dependent variation in pressure with acoustic excitation provided by either sample or window heating as described above. In our measurements with a two-resonator cell, small electret microphones were located at the longitudinal centre of each resonator with these microphone responses passed through a differential amplifier. Therefore, the quantities of interest from the frequency domain studies are the pressures at the microphone positions for the lower ($p(\vec{r}_{M,low}, \omega)$) and upper ($p(\vec{r}_{M,up}, \omega)$) resonators. We calculated $p(\vec{r}_{M,low}, \omega)$ and $p(\vec{r}_{M,up}, \omega)$ from pressure simulations by evaluating the pressure at the surface of a resonator at the position of the transverse (horizontal) mirror plane. These pressures can be positive or negative (relative to a background pressure), depending on phase. We define the differential operation response of the PA cell at a given modulation frequency as:

$$p(\vec{r}_{M,dif}) = p(\vec{r}_{M,low}) - p(\vec{r}_{M,up}) \quad 5$$

where we have omitted the angular frequency term for brevity. In addition, we append the superscripts ‘sig’ and ‘bck’ to $p(\vec{r}_{M,low})$, $p(\vec{r}_{M,up})$ and $p(\vec{r}_{M,dif})$ to denote whether excitation was provided by sample (signal) and window (background) heating, respectively. The predicted microphone responses are given by the moduli of these quantities, i.e. $|p(\vec{r}_{M,low})|$, $|p(\vec{r}_{M,up})|$ and $|p(\vec{r}_{M,dif})|$

3.2. Experimental measurements of photoacoustic cell performance

Our previous publications described our PAS instruments in detail (Cotterell et al. 2019a; Davies et al. 2018) and only a brief overview of our experimental methods is provided here. Our instrument comprised of five photoacoustic spectrometers that sampled from a common inlet, with each spectrometer driven by a separate laser. Two spectrometers operated at an optical wavelength of 405 nm, one at 514 nm and two at 658 nm. Each of the five PA cells used in experimental measurements had the same geometry as that described in the previous

section and were machined from aluminium alloy. The temperatures of all cells were controlled and maintained at 293 K using thermo-electric controllers. Measurements with flat windows used one-inch diameter N-BK7 windows (Edmund Optics), while measurements with Brewster-angled windows used UV fused silica Brewster windows (Thorlabs, BW2502). The output from a continuous-wave diode laser was directed into an astigmatic multi-pass optical cavity that provided multiple reflections (~ 50) of the laser beam through the lower resonator of the PA cell. This optical cavity was external to the cell. The intensity of the laser beam was periodically modulated at an angular frequency ω . Inlet and outlet ports were located in opposite acoustic buffer volumes and the sample flow was drawn through the cell. The design of the inlet and outlet pipes were identical to those used in our previous publications (Cotterell et al. 2019a; Davies et al. 2018, 2019; Peers et al. 2019) and consist of 0.25 inch stainless steel tubing connected to an acoustic notch filter (designed to remove acoustic noise from the sample pump) with an inner diameter twice that of the connecting 0.25 inch inlet pipe. The dimensions of the inlet system provide efficient transmission of sub-micron diameter aerosol particles; we measured the aerosol transmission efficiency for a range of mobility-selected diameter aerosols through the inlet pipe, photoacoustic cell and then the outlet, with transmission losses of $<1\%$ measured for sub-micron diameter aerosols. The sensitive microphones located at the longitudinal centre of each resonator recorded a voltage that was linearly proportional to the pressure at each microphone location. The voltage from each microphone was passed through a differential amplifier and the amplified output sent to a data acquisition (DAQ) card that recorded the microphone waveform with a time resolution of 8 MSa/s over a one-second interval.

A speaker was located close to the microphone in the lower resonator and was driven by a voltage waveform that, in the frequency domain, was a top hat distribution over the frequency range 1300 – 1700 Hz. The speaker could be used to excite a selection of cell eigenmodes. The one-second microphone time trace was recorded and processed through a Fast Fourier Transform that gave an acoustic spectrum. In this way, the resonance mode distributions in the frequency domain were measured; the resonance frequencies f_n and quality factors Q_n were determined by fitting the measured frequency-dependent $|p(\vec{r}_{M,low})|$, $|p(\vec{r}_{M,up})|$ or $|p(\vec{r}_{M,dif})|$ to equation 3.

To measure the PAS response from sample or window absorption, the microphone response was recorded for one second and processed via a Fast Fourier Transform and the frequency component of this response corresponding to the laser modulation frequency was measured. This measured photoacoustic signal is referred to as the IA. In measurements of the background photoacoustic signal (IA_{bck}) from laser-window interactions, the cell was devoid of any light absorbing sample and filled with zero air passed through a HEPA filter to remove aerosol particles and a NO_x and O_3 scrubber to remove light absorbing gases.

4. Results and discussion

We used our FEM model to understand the acoustic properties of the two-resonator PA cell. Sections 4.1 and 4.2 assess the performance of the two-resonator cell with flat and Brewster-angled windows respectively, demonstrating good agreement in acoustic properties between model predictions and measurements. Section 4.3 focusses on the optimisation of a comprehensive range of cell dimensions to maximise the SBR. Based on these optimisation studies, Sect. 4.4 examines the performance of an optimised two-resonator cell, compares model predictions with measurements and demonstrates that the detection of window background is completely suppressed.

4.1. Two-resonator PA cell with flat windows

4.1.1. The supported eigenmodes

We simulated the pressure eigenmodes $p_n(\vec{r})$ supported by the cell. We note that the model cannot identify eigenmodes that are antisymmetric about the mirror symmetry planes. Section S1 of the online Supplementary Information (SI) demonstrates the loss of identified eigenmodes with increasing mirror symmetry. In particular, the $n = 1$ mode ($f_1 \approx 600$ Hz) has antisymmetric symmetry about the transverse mirror plane and is not located when this mirror symmetry is applied. However, this mode has pressure nodes at the microphone locations and its excitation is not detectable. Moreover, this mode is not excited by a heat distribution $g(\vec{r})$ source that is symmetric about the transverse mirror plane as the overlap integral J_1 evaluates to zero. For these reasons, and that the $n = 1$ mode is well separated from other modes by >500 Hz, we ignore the $n = 1$ mode in our analysis.

Figure 3(a) shows the $p_n(\vec{r})$ for the $n = 2, 3$ eigenmodes of the flat window cell. The $n = 2$ mode is a ‘ring’ mode, with the standing wave having antinodes (pressure extremum) in each resonator of opposite phase, while a pressure node is found close to the cell windows. In the time domain, the $n = 2$ pressure oscillates with the extremum in each resonator varying in phase from $-\pi$ to $+\pi$ at a periodic frequency of $f_2 = 1355$ Hz. The $n = 3$ mode is a longitudinal mode with pressure antinodes at the window boundaries in addition to antinodes at the resonator centres. The resonance frequency of the $n = 3$ mode is $f_3 = 1502$ Hz and is separated from the f_2 resonance frequency by ~ 150 Hz. We refer to the $n = 2$ and $n = 3$ mode as the *ring* and *longitudinal* modes, respectively. It is useful to consider the physical processes that lead to the formation of the ring and longitudinal modes.

The pressure distributions of the longitudinal and ring mode are the in-phase and out-of-phase conditions for two strongly coupled open Fabry-Pérot (FP) resonators (Ward et al. 2016). In the absence of the capping buffer volumes (i.e. for a resonator opening into an infinite volume), the eigenmode of each resonator requires pressure nodes (x component of velocity field are antinodes) at its ends and an integer number of half-wavelengths supported over its length. To first order, the frequencies of the FP modes are given by $f_{FP,q} = qc/2l_{res}$, with c the speed of sound (343 ms^{-1} at room temperature and pressure) and q the FP mode order. In this way, we can predict the first ($q = 1$) FP mode to have an eigenfrequency of 1556 Hz for $l_{res} = 11$ cm, similar to the FEM prediction for the longitudinal mode. However, in this calculation we have neglected the end correction associated with evanescent wave diffraction, and it is these evanescent fields that determine whether the individual cavities are coupled to give the longitudinal (in-phase) or ring (out-of-phase) mode. We direct the reader to Ward et al. 2016 for a thorough discussion of the types of acoustic modes arising in close-lying resonator pipes, including those corresponding to the ring and longitudinal modes. We stress that the formation of the ring mode in the two resonator PA cell is unique to cells containing multiple resonators and is clearly not formed in a single-resonator PA cell.

4.1.2. Mode excitation through sample heating

We investigated the PA cell response to sample or window heating excitation, simulating the microphone responses with variation in the laser modulation frequency over the frequency range of 1300 – 1600 Hz. For sample heating, Figure 4(a) shows the predicted frequency-dependent responses for $|p^{sig}(\vec{r}_{M,low})|$, $|p^{sig}(\vec{r}_{M,up})|$ and $|p^{sig}(\vec{r}_{M,dif})|$ at frequencies close to the ring mode eigenfrequency $f_2 = 1355$ Hz. The microphone pressures at the longitudinal mode eigenfrequency ($f_3 = 1502$ Hz) were negligible and therefore the responses at frequencies >1400 Hz are not shown. Sample heating excitation at the longitudinal mode eigenfrequency is very weak for two reasons. First, Figure 3(a) shows that the longitudinal mode has relatively similar portions of positive and negative eigenmode pressure along the length of the laser beam heating volume (see also the line profile in Figure S2(a) of the SI).

Thus, the overlap integral J_3 in equation 2 evaluates to near zero. Second, the longitudinal eigenmode pressure at the two resonator centres are similar in magnitude and equal in phase, giving near-perfect subtraction of any microphone-detected excitation of the longitudinal mode for the differential amplified response.

Figure 4(a) shows that there is a significant microphone response at the ring mode eigenfrequency. This large microphone response is due to the non-zero overlap integral J_2 ; Figure 3(a) shows that the eigenmode pressure along the path length of the laser beam is always positive (see also the line profile in Figure S2(a)). Moreover, Figure 4(a) shows that the individual microphone pressure responses $|p^{sig}(\vec{r}_{M,low})|$ and $|p^{sig}(\vec{r}_{M,up})|$ are similar in amplitude. However, the phase of the ring mode pressure field at the two microphone locations is opposite and the differential response $|p^{sig}(\vec{r}_{M,dif})|$ is thus amplified. Fitting the frequency dependent $|p^{sig}(\vec{r}_{M,dif})|$ to equation 3 gives a best-fit ring mode quality factor of $Q_2 = 104.6 \pm 2.6$.

Figure 4(a) also shows the measured response for our measurement cell, averaged for the five PA spectrometers in our instrument. In these measurements, speaker excitation was used to measure the resonance mode distributions. For comparison purposes, the measured microphone response is normalised to the 27.1 μPa amplitude of the model prediction for $|p^{sig}(\vec{r}_{M,dif})|$; the microphones were not calibrated, so conversion of the measured voltages to a pressure was not possible. There is good agreement between the predicted and measured distributions, with the measured distribution having $f_2 = 1344.6 \pm 0.8$ Hz and $Q_2 = 94.5 \pm 2.7$. Our model overestimates Q_2 (underestimates thermal and viscous damping) by 10.7%, while f_2 is overestimated by 10 Hz (<1%). The reasons for these discrepancies include that our model does not include a humidity probe that protrudes into a buffer volume of our measurement cell and neglects the impedances introduced by the speaker, microphone and sample inlet/outlet ports. Moreover, additional thermal and viscous energy dissipation arises from the surfaces of the cell that our model assumes as perfectly smooth.

4.1.3. Mode excitation through window heating

Figure 4(b) shows the frequency-dependent pressure for the case of acoustic excitation from laser heating of the windows. The frequency responses $|p^{sig}(\vec{r}_{M,low})|$ and $|p^{sig}(\vec{r}_{M,up})|$ are not symmetric about the ring mode eigenfrequency, but a Lorentzian pressure distribution is recovered when the microphone responses are passed through a differential amplifier. The non-symmetric distributions for the individual microphone responses is explained by accounting for acoustic excitation of both the ring and longitudinal eigenmodes. Section S2 of the SI rationalises this non-symmetric response using an empirical model. Crucially, the J_n (i.e. the overlap integral for the pressure, absorber and laser power distributions; see Sect. 2) for window heating is ~ 60 times larger for the longitudinal compared to the ring mode. Thus, even though the longitudinal and ring eigenfrequencies are separated by 150 Hz, the strong longitudinal mode excitation gives a significant longitudinal mode contribution to the individual microphone responses at the ring mode eigenfrequency. However, the longitudinal mode contribution is almost completely removed by the differential amplifier as the longitudinal mode pressure in the two resonators have near-equal phase. Meanwhile, the ring mode contribution is amplified and a Lorentzian distribution is recovered for $|p^{sig}(\vec{r}_{M,dif})|$.

Taking the ratio of the differential-operation amplitudes $|p^{sig}(\vec{r}_{M,dif}, \omega_2)|$ and $|p^{bck}(\vec{r}_{M,dif}, \omega_2)|$ (differential microphone responses at the ring mode eigenfrequency), $\text{SBR} = 0.112$. This SBR value is useful for comparing to the performance of other cell geometries in later sections. In the discussion above, we have shown that window background sources couple very efficiently into the longitudinal mode compared to the ring mode and the

differential amplifier removes most of the longitudinal mode detection. Without differential operation, p_0^{sig} is 50% lower, while p_0^{bck} 35% higher and the SBR would be 0.042, a decrease of 63%. Therefore, it is important that researchers using the two-resonator cell design use a differential amplification detection scheme to maximise the sensitivity of their measurements.

4.2. Two-resonator PA cell with Brewster-angled windows

We now assess the performance of the two-resonator cell with Brewster windows and compare this performance with that of the flat window cell.

4.2.1. The supported eigenmodes

Figure 3(b) shows the eigenmode pressure distributions for the Brewster window cell. The eigenmode pressure distributions are similar to those for the flat window cell, although the longitudinal mode has a lower eigenfrequency for the Brewster window cell. The reduction in $n = 3$ eigenfrequency is caused by the longer length of the cell upon the inclusion of the Brewster windows, giving a longer acoustic wavelength. Meanwhile, the ring mode eigenfrequency is not sensitive to changes in window dimensions; the pressure field couples between the two resonator pipes and has minimal interaction with the window volumes. The $n = 2, 3$ eigenfrequencies are separated by only 57 Hz for the Brewster window cell, compared to a ~ 150 Hz separation for the flat window cell. This reduced frequency spacing for the Brewster cell has implications for the detection of single mode excitation.

4.2.2. Mode excitation through sample heating

Figure 5(a) compares the predicted $|p^{sig}(\vec{r}_{M,dif})|$ with the measured differential amplifier response for speaker excitation, averaged for our five PA cells. For comparison purposes, we have scaled the amplitude of the measured response to equal the amplitude of the model distribution. The measured response has a Lorentzian distribution with $f_0 = 1350.6 \pm 1.1$ Hz and $Q = 91.7 \pm 3.3$. The model predicts $f_2 = 1353.4 \pm 0.1$ Hz, larger than the measured value by 2.8 Hz, and $Q = 104.6 \pm 0.4$, larger than the measured value by 12.9. These discrepancies arise for the same reason outlined in Sect. 4.1.2; our model ignores the humidity probe that protrudes into our measurement cell and neglects the impedances from the speaker, microphones and sample inlet/outlet ports. Moreover, the measurement cells were temperature stabilised using a thermo-electric controller and, while we performed both our simulations and experimental measurements for a temperature of 293.15 K, systematic biases in the cell temperature are possible. If the 2.8 Hz discrepancy in f_2 between model and measurement were caused exclusively by a systematic error in temperature, the temperature bias would have to be 1.3 K, with experimental biases in temperature of ~ 1 K possible. In particular, our temperature control uses a thermistor embedded within the wall of the aluminium-alloy cell and the internal air temperature was not measured directly.

4.2.3. Mode excitation through window heating

Figure 5(b), (c) and (d) show predictions of $|p^{bck}(\vec{r}_{M,low})|$, $|p^{bck}(\vec{r}_{M,up})|$ and $|p^{bck}(\vec{r}_{M,dif})|$, respectively, compared with measurements using our spectrometers with either 405, 514 or 658 nm laser excitation. Measurements using our second 658-nm PA spectrometer are not shown due to a faulty laser at the time of measurement. There is good agreement between model predictions and measurements for both individual microphone and differential responses. For the individual microphone responses, the simulations agree well with the measured response, even showing subtle features such as the contribution of ring mode excitation in the 1340 – 1360 Hz range. For $|p^{bck}(\vec{r}_{M,dif})|$, the ring mode excitation is amplified while the longitudinal mode excitation from the individual microphone responses is partly removed. To rationalise the incomplete removal of longitudinal mode detection in the

differential response, Figure S3 shows line profiles through the $n = 3$ pressure eigenmode distribution for profiles through both the upper and lower resonators. For both Brewster-angled and flat windows, the eigenmode pressure at the microphone position ($x = 0$) is more negative in the lower compared to the upper resonator. However, the difference in eigenmode pressure between the two microphones is larger for the Brewster window cell compared to that using flat windows. This larger difference in $p_{n=3}(\vec{r}_M)$ for the Brewster window cell corresponds to a small difference in phase, leading to incomplete removal of longitudinal mode detection by the differential amplifier.

Our model agrees well with the window heating measurements in Figure 5 for the ring mode excitation, while the longitudinal mode eigenfrequency is predicted to be slightly larger than the measured values. The average measured longitudinal mode eigenfrequency is 1395.6 ± 5.2 Hz, lower than the predicted value by 14.4 Hz. Even in the measured data for our four PA cells, the $n = 3$ eigenfrequency varies considerably and cannot be rationalised by variations in cell temperature. We show in Sect. 4.3.1. that the longitudinal mode eigenfrequency is very sensitive to small variations in the length of the buffer volumes; a 1 mm increase in l_{buf} is predicted to decrease the longitudinal mode eigenfrequency by 7.7 Hz. Therefore, a +2 mm error in the buffer lengths could be responsible for the 14 Hz eigenfrequency discrepancy. Meanwhile, discrepancies between measured and predicted longitudinal mode amplitudes are likely caused by small differences in sensitivity for the upper and lower microphones.

We can estimate the contribution of $n = 3$ mode excitation to detection of window background at the $n = 2$ eigenfrequency by fitting the predicted $|p^{bck}(\vec{r}_{M,dif}, \omega)|$ to a bimodal distribution consistent with equation 1:

$$|p(\vec{r}_M, \omega)| = A_2 \sqrt{\frac{1}{1+Q_2^2(\frac{f_2-f}{f_2})^2}} + A_3 \sqrt{\frac{1}{1+Q_3^2(\frac{f_3-f}{f_3})^2}} \quad 6$$

in which A_n are the amplitude contributions of the $n = 2, 3$ modes. We used a least-squares routine that varied A_n, f_n and Q_n for each mode to fit equation 6 to the predicted $|p^{bck}(\vec{r}_{M,dif}, \omega)|$. Figure S4 compares this best-fit distribution to $|p^{bck}(\vec{r}_{M,dif}, \omega)|$. The best-fit of this bimodal distribution indicates that longitudinal mode excitation represents 7.5 % of the window background microphone response at the ring mode eigenfrequency. Therefore, the contribution from longitudinal mode excitation to $|p^{bck}(\vec{r}_{M,dif})|$ at the ring mode eigenfrequency is small.

From taking the amplitudes of $|p^{sig}(\vec{r}_{M,dif})|$ and $|p^{bck}(\vec{r}_{M,dif})|$ at the ring mode eigenfrequency, the FEM simulations predict $SBR = 0.026$. Importantly, the predicted SBR for the Brewster window cell is smaller than that for the corresponding flat window cell ($SBR = 0.112$) using the same model parameters, i.e. the performance for the Brewster cell is predicted to be worse. Figure S5 compares the frequency-dependent $|p^{sig}(\vec{r}_{M,dif})|$ and $|p^{bck}(\vec{r}_{M,dif})|$ for both cases of Brewster or flat windows. The amplitude of $|p^{sig}(\vec{r}_{M,dif})|$ decreased by 10% when including Brewster windows and $|p^{bck}(\vec{r}_{M,dif})|$ increased by 300%. However, Figure S6 demonstrates that we measured a >50 % reduction in $|p^{bck}(\vec{r}_{M,dif})|$ when using Brewster-angled rather than flat windows. This difference between experiment and simulation arises because our model does not account for the reduced laser-window interaction when using Brewster windows. Our model compares the acoustic response for different cells on geometry grounds alone and differences in window materials and transmission/scattering are not considered. Therefore, Brewster windows should be used to improve the sensitivity and SBR in PAS measurements using the two-resonator cell geometry.

4.3. Optimising the PA cell geometry

We used our model to optimise the geometry of our two-resonator cell. Henceforth, all cell geometries included Brewster windows because our measurements discussed above have demonstrated a significant reduction in the window background compared to using flat windows. There are multiple dimensions of the cell to consider optimising, including those of the buffer volume (l_{buf} , h_{buf} , w_{buf} and r_{fil}) and the inter-resonator separation (d_{res}). We did not consider optimising the dimensions of the window volumes as these were governed by the sizes of Brewster windows available. Moreover, we did not consider varying the lower resonator radius; decreasing this radius is not desirable as this needs to remain large enough for our multipass laser beam to pass through the resonator, while previous studies show that larger values increase sensitivity to laser-window interactions (Cotterell et al. 2019b; Bijnen et al. 1996).

The sections below consider the impact on cell performance of varying l_{buf} (Sect. 4.3.1.), simultaneously varying h_{buf} and w_{buf} (Sect. 4.3.2.), varying r_{fil} (Sect. 4.3.3.), and simultaneously varying d_{res} and $r_{res,up}$ (the upper resonator radius, Sect. 4.3.4.). In these simulations, all other cell dimensions remained fixed at the values in Table 1. While we appreciate that there will be interdependencies between all geometric quantities, it was not possible to optimise all dimensions of the cell with our limited computational power. Our optimisation studies provide an indication of the ideal two-resonator cell geometry.

4.3.1. Optimising the length of the buffer volumes

We varied l_{buf} from $0.3l_{res}$ to $0.7l_{res}$ in $0.1l_{res}$ intervals (with $l_{res} = 11$ cm, see Table 1). Our previous optimisation studies for a single-resonator cell (Cotterell et al. 2019b) found the SBR was maximised, and $|p^{bck}(\vec{r}_{M,dif})|$ minimised, for $l_{buf} = 0.5l_{res}$, i.e. the buffer length currently used in our two-resonator cell. Indeed, Bijnen *et al.* has also found $l_{buf} = 0.5l_{res}$ to be the optimal buffer length for a single-resonator cell (Bijnen *et al.* 1996).

Figure 6 shows the pressure eigenmode distributions for the ring and longitudinal modes with varying l_{buf} , with the colour scale on these plots expanded to emphasise key variations in $p_n(\vec{r})$ with increasing l_{buf} . As l_{buf} increases, the ring mode eigenfrequency does not change while the longitudinal eigenfrequency decreases significantly. The longitudinal mode is the $n = 3$ eigenmode at $l_{buf} = 0.3l_{res}$, but is the $n = 2$ eigenmode at $l_{buf} = 0.6l_{res}$. The sensitivity of the longitudinal mode eigenfrequency is -7.7 Hz per 1 mm increase in l_{buf} . This sensitivity is expected to account for the measured variability in the longitudinal eigenfrequency reported in Sect. 4.2.3.

Figure 7 shows the predicted $|p^{sig}(\vec{r}_{M,dif})|$ and $|p^{bck}(\vec{r}_{M,dif})|$ over the frequency range 1320 – 1380 Hz for different l_{buf} values. For sample heating, there is little influence of l_{buf} on the excitation amplitude. For window heating, the $|p^{bck}(\vec{r}_{M,dif}, \omega)|$ show non-Lorentzian behaviour caused by efficient excitation of both the longitudinal and ring modes; as discussed earlier, the overlap integral J_n for the longitudinal mode is large for the case of window heating. Importantly, the amplitude of $|p^{bck}(\vec{r}_{M,dif})|$ at the ring mode eigenfrequency decreases significantly with increasing l_{buf} to nearly zero for $l_{buf} = 0.7l_{res}$. Indeed, the amplitude of $|p^{bck}(\vec{r}_{M,dif})|$ for the $l_{buf} = 0.7l_{res}$ model distribution cannot be resolved on the axis scale of Figure 7(b). To explain the rapid decrease in background with increasing l_{buf} , the eigenmode pressure distributions in Figure 6(a) demonstrate that the $p_n(\vec{r})$ for the ring mode within the window volumes is non-zero for $l_{buf} = 0.3l_{res}$ but decreases rapidly to zero as l_{buf} tends to $0.7l_{res}$. Moreover, there is also a progressive reduction in detection of longitudinal mode excitation. To explain this latter phenomenon, the eigenmode pressure distributions in Figure 6(b) for the longitudinal mode show that the $p_n(\vec{r})$ are not equal at the location of the lower

and upper microphones for $l_{buf} = 0.3l_{res}$ and there is imperfect subtraction of detected longitudinal mode excitations upon passing the microphone signals through a differential amplifier. As l_{buf} increases, the $p_n(\vec{r})$ at the two microphone positions become equal and the differential amplifier completely removes detection of the longitudinal mode excitation.

We calculated the SBR from the amplitudes of $|p^{sig}(\vec{r}_{M,dif})|$ and $|p^{bck}(\vec{r}_{M,dif})|$ at the ring mode eigenfrequency and Figure 7(c) shows the dependence of SBR on l_{buf} . The SBR progressively increases with l_{buf} to $SBR > 5$ at $l_{buf} = 0.7l_{res}$. Crucially, a 2 cm increase in l_{buf} from the $l_{buf} = 0.5l_{res}$ value for our current measurement cell is expected to suppress the dominant background contribution arising from laser-window interactions. Moreover, this result demonstrates that the general rule of setting $l_{buf} = l_{res}/2$ is not a universal design criteria and it is important to solve rigorously the thermoviscous acoustics to determine optimal cell dimensions.

4.3.2. Optimising the height and width of the buffer volumes

We investigated the impact of varying the buffer height (h_{buf}) and width (w_{buf}) on cell performance. The current cell has $h_{buf} = 4.2$ cm and $w_{buf} = 2.6$ cm. Given the resonator radii ($r_{res} = 1.0$ cm) and their centre-to-centre separation ($d_{res} = 2.2$ cm), we were restricted to lower limits of $h_{buf} = 4.2$ cm and $w_{buf} = 2.0$ cm. The simulations reported here varied h_{buf} from 4.5 cm to 6 cm in 0.5 cm steps, while w_{buf} was varied from 2.5 cm to 4 cm in 0.5 cm steps.

Figure 8 summarises the amplitudes in the $|p^{sig}(\vec{r}_{M,dif}, \omega_n)|$ and $|p^{bck}(\vec{r}_{M,dif}, \omega_n)|$ with variation in w_{buf} and h_{buf} (frequency-dependent excitation curves are provided in Figure S7 and S8). For sample heating, changing w_{buf} or h_{buf} had no impact on the $|p^{sig}(\vec{r}_{M,dif}, \omega_n)|$. For window heating, $|p^{bck}(\vec{r}_{M,dif}, \omega_n)|$ decreased as w_{buf} increased and eigenmode simulations show that this decrease is caused by a reduction in ring eigenmode pressure within the window volumes. Meanwhile, $|p^{bck}(\vec{r}_{M,dif}, \omega_n)|$ increased for larger h_{buf} and eigenmode simulations show an increased ring eigenmode pressure in the window volumes for larger h_{buf} .

Figure 8(c) shows the variation in SBR with w_{buf} and h_{buf} , while Figure S9 shows a contour plot of SBR with variation in w_{buf} and h_{buf} . Increasing w_{buf} is beneficial to PA cell performance, suppressing window background and increasing the SBR. For $h_{buf} = 4.5$ cm, increasing w_{buf} by 1 cm from 2.5 to 3.5 cm increases the SBR by 0.014 (i.e. by 60%). This is a significant increase in SBR, although not as large as the ~130% improvement seen with increasing l_{buf} from 5.5 cm to 6.6 cm. Meanwhile, h_{buf} should be set as small as possible. There is scope to reduce h_{buf} by only 1 mm in our current cells if d_{res} and r_{res} are kept the same, with a 1 mm reduction in h_{buf} predicted to have a negligible impact on SBR.

Improving SBR by increasing w_{buf} or l_{buf} would necessarily increase the cell volume and therefore increase sample residence time. For a 1 L min^{-1} sample flow rate, the residence time of our current cell is ~12 s. For a 2 cm increase in l_{buf} (as recommended in Sect. 4.3.1.) and a 1 cm increase in w_{buf} , the cell response time increases to ~18 s. This larger cell response time is not desirable. One strategy to reduce the cell volume is to increase the fillet radii (r_{fil}) for the buffer volumes, although the impact of varying fillet radius on SBR needs to be assessed. Another strategy is to reduce the radius of the upper resonator pipe. In the following sections, we investigate these strategies for reducing the cell volume and their impact on SBR.

4.3.3. Optimising the fillet radius of the buffer volume

The current two-resonator cell has $r_{fil} = 0.8$ cm. In our model, we studied the impact on the microphone responses and SBR of varying r_{fil} from 0.65 cm ($0.5w_{buf}/2$) to 1.18 cm ($0.9w_{buf}/2$) in 0.13 cm ($0.1w_{buf}/2$) intervals. Figure S10 shows cross sections of the buffer volumes tested

in this study and indicates how the total cell volume changes with r_{fil} , while Figure S11 shows calculations of $|p^{sig}(\vec{r}_{mic,dif}, \omega)|$, $|p^{bck}(\vec{r}_{mic,dif}, \omega)|$, SBR and response time with variation in r_{fil} . As r_{fil} increases from 0.65 cm to 1.18 cm, the total cell volume decreases by 4.3%. The ring mode excitation amplitude from sample heating is invariant with increasing r_{fil} , while the response from window heating shows a small decrease. The SBR increases from 0.027 to 0.032 as r_{fil} increases from 0.78 cm to 1.18 cm. For the same change in r_{fil} , there is a modest improvement in cell response time of 0.4 s. Thus, we recommend using a buffer volume with r_{fil} set as large as permitted by the cell geometry, with r_{fil} limited in our cell by the radius of the resonators and the resonator separation d_{res} to a maximum value of $\sim r_{fil} = 0.9w_{buf}/2$.

4.3.4. Optimising the upper resonator radius and the resonator separation distance

Here, we consider the possibility of reducing the cell volume by decreasing the radius of the upper resonator ($r_{res,up}$). The radius of the lower resonator is restricted to $r_{res,low} \approx 1.0$ cm by the need to propagate a multipass beam through the resonator, but the same constraint does not apply to the upper resonator. We used our FEM model to study the performance of the two-resonator cell for $r_{res,up}$ values ranging from $0.5r_{res,low}$ to $0.9r_{res,low}$ in $0.2r_{res,low}$ intervals. Smaller values of $r_{res,up}$ also allow the centre-to-centre resonator separation d_{res} to be reduced. Therefore, we varied d_{res} for each of the aforementioned values of $r_{res,up}$, with d_{res} taking values of 1.8 cm, 2.0 cm and 2.3 cm.

Figure S12 shows how $|p^{sig}(\vec{r}_{M,dif}, \omega_n)|$, $|p^{bck}(\vec{r}_{M,dif}, \omega_n)|$ and SBR vary with $r_{res,up}$ and d_{res} . We also include on these plots the values for the current cell geometry (with $r_{res,up} = r_{res,low}$ and $d_{res} = 2.2$ cm) in addition to a point that has the same geometry as the current cell albeit with a larger upper resonator radius ($r_{res,up} = 1.1r_{res,low}$). Meanwhile, Figure S13 shows the variations in the eigenmode pressure distributions for the ring and longitudinal modes for the ranges of $r_{res,up}$ and d_{res} input to the model. There is very little variation in the sample heating signal with changes in either $r_{res,up}$ or d_{res} . For window heating, $|p^{bck}(\vec{r}_{M,dif}, \omega_n)|$ depends strongly on $r_{res,up}$ and is minimised (SBR is maximised) for $r_{res,up} = r_{res,low}$, i.e. when the two resonators have the same dimensions. Indeed, the SBR is an order of magnitude higher when the resonators have equal radii compared to when $r_{res,up} = 0.5r_{res,low}$. The eigenmode simulations show that the decrease in $|p^{bck}(\vec{r}_{M,dif}, \omega_n)|$ as $r_{res,up}$ tends to $r_{res,low}$ is associated with a reduced ring mode $p_n(\vec{r})$ in the window volumes. Furthermore, the pressures at the two microphone locations become more similar for the longitudinal mode, leading to more effective removal of longitudinal mode detection by the differential amplifier. For the narrow 5 mm range of d_{res} input to the FEM model, Figure S12 shows that there is only a small improvement in SBR by setting d_{res} as large as possible, with the maximum d_{res} limited by the buffer height. We performed simulations to investigate the impact of larger values of h_{buf} , on the SBR with d_{res} set to the maximum value (see Figure S14). However, the results of these simulations continue to support the conclusion that h_{buf} should be kept as small as possible (as was concluded in Sect. 4.3.2) with d_{res} set to the maximum value.

4.3.5. Optimising the buffer and resonator lengths for a conserved total cell length

The key conclusions from the studies above are: (1) The buffer length should be increased from the current value of $0.5l_{res}$ to $0.7l_{res}$. This increase in l_{buf} improved the SBR by a factor of 200. (2) Increasing w_{buf} by 1 cm increased the SBR by 60%. This is a small impact on SBR compared to that achieved by increasing l_{buf} , while a larger w_{buf} will increase sample residence time. Therefore, we suggest keeping w_{buf} unchanged. (3) h_{buf} should be kept as small as possible, while d_{res} should be set as large as possible. (4) r_{fil} should be set as large as permitted by the geometry of the model, with r_{fil} limited by the radius of the resonators and the resonator separation d_{res} to a maximum value of $\sim r_{fil} = 0.9w_{buf}/2$. (5) The resonator radii must be equal for both resonators.

Using these design principles as a guide, we consider the dimensions of a candidate cell. We set the buffer dimensions to $w_{buf} = 2.6$ cm (unchanged), $h_{buf} = 4.1$ cm (set to minimum value) and $r_{fil} = 1.2$ cm. For the resonator dimensions, $d_{res} = 2.1$ cm and the resonator radii were reduced only slightly to 0.9 cm. The latter reduction in r_{res} helped reduce the total cell volume and previous studies show that smaller resonator radii improve the SBR (Cotterell et al. 2019b; Bijnen et al. 1996), while a resonator radius of 0.9 cm remains large enough for our multipass laser beam to pass through the lower resonator. For the buffer length, the available space in our own instrument was restricted and making the cell longer, thus achieving criteria (1) above, was not possible. However, we note that we have not considered in our optimisation studies the effect of varying the resonator lengths; l_{buf} could be increased at the expense of reducing the resonator length and the total cell length of 22 cm conserved through the equation:

$$l_{buf} = \frac{22.0 \text{ cm} - l_{res}}{2} \quad 7$$

Thus, we performed simulations of the cell acoustic performance using the dimensions specified above and varied l_{res} from 8 cm to 11 cm with the total cell length constrained to 22 cm using equation 7, varying the ratio l_{buf}/l_{res} over the range 0.50 – 0.88. Figure S15 shows the eigenmode pressure distributions for the ring and longitudinal mode. The ring mode pressure distributions show that the eigenmode pressure within the window heating volume is close to zero for $l_{buf}/l_{res} = 0.7$ ($l_{res} = 9.2$ cm, $l_{buf} = 6.4$ cm). Figure S16 shows the $|p^{sig}(\vec{r}_{mic,dif}, \omega)|$ and $|p^{bck}(\vec{r}_{mic,dif}, \omega)|$ for sample and window heating respectively, with simulations performed over the reduced l_{buf}/l_{res} range of 0.65 - 0.75 owing to the computational expense of calculating microphone responses for sample and window heating. While there are small variations in the sample heating amplitude at the ring mode frequency, the corresponding window heating amplitudes show significant variation. Importantly, Figure 9(a) shows that the SBR is maximised for $l_{buf}/l_{res} = 0.7$, consistent with the optimal l_{buf}/l_{res} ratio found in Sect. 4.3.1. for when the total cell length was not constrained and $l_{res} = 11$ cm. Figure 9(a) shows that the candidate cell with $l_{buf}/l_{res} = 0.7$ has an SBR of 4.35, an improvement of a factor of 170 over our current cell ($l_{res} = 11$ cm, $l_{buf}/l_{res} = 0.5$). Furthermore, Figure 9(b) and (c) compare the predicted frequency-dependent differential operation responses for this optimised cell with our original cell for both sample and window heating. At the ring mode eigenfrequency, the sample heating response for the optimised cell is unchanged from that of the original cell, while the window heating response is suppressed by a factor of 170 for the optimised cell. In addition to the superior SBR, the optimised cell has a reduced response time of 11.4 s for a 1 L min⁻¹ sample flow rate, 5% lower than the 12 s response time for the original cell.

4.4. An optimised two-resonator PA cell: model vs measurement

We now define the final dimensions of our optimised PA cell, using the same dimensions as used in Sect. 4.3.6., with $l_{res} = 9.2$ cm and $l_{buf} = 6.4$ cm. The dimensions of the optimised cell are summarised in Table 2. We manufactured this cell from aluminium-alloy (Tarvin Precision Limited) and measured the cell acoustic behaviour, comparing measurements with our model predictions. We recorded the microphone responses for laser heating of the cell windows, with the cell devoid of any light absorbing sample. For these measurements, the laser amplitude modulation frequency was set to the ring mode eigenfrequency that was measured as 1604 Hz using speaker excitation of the cell. We used the same multipass optical set-up as in measurements above, using lasers with either a 405 or 658 nm optical wavelength and output powers of 260 and 100 mW, respectively. Ambient air was drawn through a Nafion dryer, NO₂ and O₃ scrubber and then the PAS cell at a flow rate of 1 L min⁻¹. We performed pressure stability tests to ensure that the cell and flow system were leak tight. The temperature of the PAS cell was maintained at 21 °C using a thermoelectric controller.

For window heating, Figure 10(a) shows the measured IA values for the original and optimised cells for laser wavelengths of 405 and 658 nm. For the original cell, IA_{bck} takes values of 6.39 and 3.28 at the 405 and 658 nm wavelengths, respectively. We note that the imaginary refractive index (directly proportional to the material absorption coefficient) for glasses tend to increase significantly as the optical wavelength approaches the UV spectrum. This increase in glass absorption is likely responsible for the larger IA_{bck} at 405 nm, while we also note that we observe increased scattering at the window surfaces at shorter laser wavelengths. Both the increased absorption and scattering of light at shorter wavelengths likely contribute to larger IA_{bck} at 405 nm compared to that at the 658 nm wavelength. The IA_{bck} for the optimised cell is a factor of 48 and 24 lower than that for the original cell at the 405 and 658 nm laser wavelengths respectively. These levels of suppression in IA_{bck} differ from the predicted suppression in window background by a factor of 170; as we show below, IA_{bck} approaches a sensitivity threshold limited by ambient noise, a threshold that is not considered in our model. Crucially, the uncertainties in IA_{bck} for the optimised cell are within the measured IA uncertainty for measurements absent of any laser excitation (laser off), i.e. when the microphone response is dominated by ambient noise associated with sample flow, instrument vibrations and electronic noise in the microphone measurements. Figure 10(b) demonstrates further the statistical insignificance of IA_{bck} for the optimised cell compared to ambient noise, showing a time series in IA for a 120 s period with the laser off and then for a 120 s period with the laser on. This figure also includes an indicative scale for absorption coefficient, demonstrating that the instrument sensitivity is $<0.5 \text{ Mm}^{-1}$ and is limited by the ambient noise in microphone measurements.

We also recorded IA_{bck} with variation in the laser modulation frequency for both the signal microphone, reference microphone and for when the microphone signals were passed through a differential amplifier. The laser frequency was increased in 10 Hz intervals over the frequency range 1450 – 1650 Hz and IA_{bck} was recorded for 30 s at each frequency and the mean value calculated. Figure 11(a) compares the measured responses for the two individual microphones with the predicted response. The measured and predicted responses are in good agreement. There are small differences between the two microphone responses at the ring mode eigenfrequency (measured as 1604 Hz), with the signal microphone response increased and the reference microphone decreased compared to the model prediction. This small difference in behaviour is associated with an increased excitation of the ring mode that is not included in the FEM model, with contributions from the incomplete suppression in the detection of laser-window interactions and from ambient noise. The trends in the individual microphone responses with frequency were discussed in Sect. 4.1.1. and is caused by the antiphase ring mode pressures at the two microphone locations; any ring mode excitation adds to the longitudinal mode contribution for the signal microphone response and subtracts from the longitudinal mode contribution for the reference microphone. Figure 11(b) compares the predicted and measured differential amplifier response. Again, the trends in the model predictions with changing frequency agree well the measured response.

Finally, Sect. 4.3.5 showed that our FEM model predicted the sample heating response for the optimised cell to be unchanged from that of the original cell at the ring mode eigenfrequency. Therefore, we also performed experimental measurements to confirm that the photoacoustic responses for sample heating were similar for the optimised and original cells. Previous work has comprehensively demonstrated that using ozone gas as a calibrant is an effecting approach for accurate calibration of aerosol PAS instruments (Cotterell et al. 2019a; Davies et al. 2018). Here, ozone gas is passed first through a cavity ring-down spectrometer for direct measurement of the ozone absorption coefficient prior to the ozone sample passing via serial flow to the PAS instrument for measurement of the photoacoustic response. The reader is directed to Davies et al. 2018 and Cotterell et al. 2019a for full details of our calibration procedure using this approach. Figure S17 shows that, for the same concentration of ozone

gas, the photoacoustic response of the optimised cell is 11% lower than that of the original cell. We note that the measurements using the two different cells required the multipass laser optics to be re-aligned upon installation of the new cell. This re-alignment causes small changes to the overlap integral J_n , which subsequently leads to small variations in the calibration coefficient. This change in J_n largely accounts for the 11% difference in calibration coefficient.

5. Summary

We have used finite element modelling to understand the acoustic behaviour of a common two-resonator photoacoustic cell that is used by many research groups for the measurement of aerosol absorption coefficients. Our model predictions of photoacoustic pressure at the microphone locations are in excellent agreement with measurements, and understanding this acoustic response requires us to consider the excitation of both a ring and longitudinal mode. In particular, laser-window interaction sources excite the longitudinal mode very efficiently compared to the ring mode, with the longitudinal mode having a very large eigenmode pressure amplitude (thus a large overlap integral J_n) in the window volumes. However, the differential amplifier removes most of the microphone response corresponding to the excited longitudinal mode. Without differential operation, the signal-to-background ratio is reduced by 63%, thereby degrading the sensitivity of the PAS instrument.

We used our FEM model to optimise the geometry of the two-resonator cell, varying the dimensions of the resonators and their capping buffer volumes to maximise the SBR. In this way, we tested a very large set of cell geometries that would have taken considerable time if each cell was manufactured and tested in the laboratory. In particular, the SBR is very sensitive to the length of the buffer volumes; the SBR was increased by a factor of 150 – 200 from setting $l_{buf} = 0.7l_{res}$ compared to the $l_{buf} = 0.5l_{res}$ for our existing cell. This optimal value for l_{buf} challenges common misconceptions that the acoustic buffer volumes should be set at $l_{buf} = 0.5l_{res}$ (so-called quarter wavelength filters). Indeed, we recommend that for all but the simplest cell geometries, researchers model the acoustic behaviour for their particular cell rather than relying on general design rules. Our studies show that optimisation of other cell dimensions had significantly less impact on SBR compared to varying l_{buf} . We measured the acoustic response of an optimised cell that was used to validate model predictions. The optimised cell suppresses the detection of laser-window interactions to a level that is within measurement uncertainty, negating the need to perform a background subtraction on aerosol photoacoustic measurements, particularly during aircraft field studies for which the window background depends strongly on pressure.

Acknowledgements

This work was supported through a Royal Society of Chemistry/Analytical Chemistry Trust Fund Tom West Fellowship awarded to Michael I. Cotterell. Jim M. Haywood and Michael I. Cotterell thank the Natural Environment Research Council for support through the CLARIFY-2017 grant (NE/L013797/1). The Met Office funded experimental measurements. The Research Council on Norway provided further instrument support via the projects AC/BC (240372) and NetBC (244141).

Competing interests

The authors declare that they have no conflict of interest.

Data availability

For data related to this paper, please contact Michael I. Cotterell (m.cotterell@exeter.ac.uk).

References

- Ajtai, T., Filep, Á., Schnaiter, M., Linke, C., Vragel, M., Bozóki, Z., Szabó, G., and Leisner, T. (2010). A novel multi-wavelength photoacoustic spectrometer for the measurement of the UV-vis-NIR spectral absorption coefficient of atmospheric aerosols. *J. Aerosol Sci.*, 41(11):1020–1029.
- Alexander, N., Allen, S., Stocker, T.F., Qin, D., Plattner, G.-K., Trignor, M.M.B., Boschung, J., Xia, Y., Bex, V., and Midgley, P.M. (2013). Working Group I Contribution to the Fifth Assessment Report of the Intergovernmental Panel on Climate Change.
- Arnott, W.P., Walker, J.W., Moosmüller, H., Elleman, R.A., Jonsson, H.H., Buzorius, G., Conant, W.C., Flagan, R.C., and Seinfeld, J.H. (2006). Photoacoustic insight for aerosol light absorption aloft from meteorological aircraft and comparison with particle soot absorption photometer measurements: DOE Southern Great Plains climate research facility and the coastal stratocumulus imposed perturbation. *J. Geophys. Res.*, 111(D5):D05S02, 1-16.
- Bijnen, F.G.C., Reuss, J., and Harren, F.J.M. (1996). Geometrical Optimization of a Longitudinal Resonant Photoacoustic Cell for Sensitive and Fast Trace Gas Detection. *Rev. Sci. Instrum.*, 67(8):2914–2923.
- Bluvshstein, N., Flores, J.M., He, Q., Segre, E., Segev, L., Hong, N., Donohue, A., Hilfiker, J.N., and Rudich, Y. (2017). Calibration of a multi-pass photoacoustic spectrometer cell using light-absorbing aerosols. *Atmos. Meas. Tech.*, 10(3):1203–1213.
- Bluvshstein, N., Michel Flores, J., Segev, L., and Rudich, Y. (2016). A new approach for retrieving the UV-vis optical properties of ambient aerosols. *Atmos. Meas. Tech.*, 9(8):3477–3490.
- Cappa, C.D., Lack, D.A., Burkholder, J.B., and Ravishankara, A.R. (2008). Bias in Filter-Based Aerosol Light Absorption Measurements Due to Organic Aerosol Loading: Evidence from Laboratory Measurements. *Aerosol Sci. Technol.*, 42(12):1022–1032.
- Cotterell, M.I., Orr-Ewing, A.J., Szpek, K., Haywood, J.M., and Langridge, J.M. (2019a). The impact of bath gas composition on the calibration of photoacoustic spectrometers with ozone at discrete visible wavelengths spanning the Chappuis band. *Atmos. Meas. Tech.*, 12(4):2371–2385.
- Cotterell, M.I., Ward, G.P., Hibbins, A.P., Haywood, J.M., Wilson, A., and Langridge, J.M. (2019b). Optimizing the Performance of Aerosol Photoacoustic Cells for Sensitive Measurements of Aerosol Light Absorption using a Finite Element Model. Part 1: Method Validation and Application to Single-Resonator Multipass Cells. *Aerosol Sci. Technol.*, in review.
- Davies, N.W., Cotterell, M.I., Fox, C., Szpek, K., Haywood, J.M., and Langridge, J.M. (2018). On the accuracy of aerosol photoacoustic spectrometer calibrations using absorption by ozone. *Atmos. Meas. Tech.*, 11(4):2313–2324.
- Davies, N.W., Fox, C., Szpek, K., Cotterell, M.I., Taylor, J.W., Allan, J.D., Williams, P.I., Trembath, J., Haywood, J.M., and Langridge, J.M. (2019). Evaluating biases in filter-based

aerosol absorption measurements using photoacoustic spectroscopy. *Atmos. Meas. Tech.*, 12(6):3417–3434.

Fischer, D. and Smith, G.D. (2018a). A portable, four-wavelength, single-cell photoacoustic spectrometer for ambient aerosol absorption. *Aerosol Sci. Technol.*, 52(4):393–406.

Fischer, D. and Smith, G.D. (2018b). Can ozone be used to calibrate aerosol photoacoustic spectrometers? *Atmos. Meas. Tech.*, 11(12):6419–6427.

Foster, K., Pokhrel, R., Burkhardt, M., and Murphy, S. (2019). A novel approach to calibrating a photoacoustic absorption spectrometer using polydisperse absorbing aerosol. *Atmos. Meas. Tech.*, 12(6):3351–3363.

Krämer, L., Bozoki, Z., and Niessner, R. (2001). Characterisation of a mobile photoacoustic sensor for atmospheric black carbon monitoring. *Anal. Sci.*, 17(April):s563–s566.

Lack, D.A., Cappa, C.D., Covert, D.S., Baynard, T., Massoli, P., Sierau, B., Bates, T.S., Quinn, P.K., Lovejoy, E.R., and Ravishankara, A.R. (2008). Bias in filter-based aerosol light absorption measurements due to organic aerosol loading: Evidence from ambient measurements. *Aerosol Sci. Technol.*, 42(12):1033–1041.

Lack, D.A., Cappa, C.D., Cross, E.S., Massoli, P., Ahern, A.T., Davidovits, P., and Onasch, T.B. (2009). Absorption Enhancement of Coated Absorbing Aerosols: Validation of the Photo-Acoustic Technique for Measuring the Enhancement. *Aerosol Sci. Technol.*, 43(10):1006–1012.

Lack, D.A., Lovejoy, E.R., Baynard, T., Pettersson, A., and Ravishankara, A.R. (2006). Aerosol Absorption Measurement using Photoacoustic Spectroscopy: Sensitivity, Calibration, and Uncertainty Developments. *Aerosol Sci. Technol.*, 40(9):697–708.

Lack, D.A., Richardson, M.S., Law, D., Langridge, J.M., Cappa, C.D., McLaughlin, R.J., and Murphy, D.M. (2012). Aircraft Instrument for Comprehensive Characterization of Aerosol Optical Properties, Part 2: Black and Brown Carbon Absorption and Absorption Enhancement Measured with Photo Acoustic Spectroscopy. *Aerosol Sci. Technol.*, 46(5):555–568.

Laskin, A., Laskin, J., and Nizkorodov, S.A. (2015). Chemistry of Atmospheric Brown Carbon. *Chem. Rev.*, 115(10):4335–4382.

Linke, C., Ibrahim, I., Schleicher, N., Hitzenberger, R., Andreae, M.O., Leisner, T., and Schnaiter, M. (2016). A novel single-cavity three-wavelength photoacoustic spectrometer for atmospheric aerosol research. *Atmos. Meas. Tech.*, 9(11):5331–5346.

Miklós, A., Hess, P., and Bozóki, Z. (2001). Application of acoustic resonators in photoacoustic trace gas analysis and metrology. *Rev. Sci. Instrum.*, 72(4):1937–1955.

Moise, T., Flores, J.M., and Rudich, Y. (2015). Optical Properties of Secondary Organic Aerosols and Their Changes by Chemical Processes. *Chem. Rev.*, 115(10):4400–4439.

Moosmüller, H., Chakrabarty, R.K., and Arnott, W.P. (2009). Aerosol light absorption and its measurement: A review. *J. Quant. Spectrosc. Radiat. Transf.*, 110(11):844–878.

- Nakayama, T., Kondo, Y., Moteki, N., Sahu, L.K., Kinase, T., Kita, K., and Matsumi, Y. (2010). Size-dependent correction factors for absorption measurements using filter-based photometers: PSAP and COSMOS. *J. Aerosol Sci.*, 41(4):333–343.
- Nakayama, T., Suzuki, H., Kagamitani, S., Ikeda, Y., Uchiyama, A., and Matsumi, Y. (2015). Characterization of a Three Wavelength Photoacoustic Soot Spectrometer (PASS-3) and a Photoacoustic Extinctionmeter (PAX). *J. Meteorol. Soc. Japan. Ser. II*, 93(2):285–308.
- Peers, F., Francis, P., Fox, C., Abel, S.J., Szpek, K., Cotterell, M.I., Davies, N.W., Langridge, J.M., Meyer, K.G., Platnick, S.E., and Haywood, J.M. (2019). Observation of absorbing aerosols above clouds over the South- East Atlantic Ocean from the geostationary satellite SEVIRI Part 1: Method description and sensitivity. *Atmos. Chem. Phys. Discuss.*, (January):1–24.
- Radney, J.G. and Zangmeister, C.D. (2015). Measurement of Gas and Aerosol Phase Absorption Spectra across the Visible and Near-IR Using Supercontinuum Photoacoustic Spectroscopy. *Anal. Chem.*, 87(14):7356–7363.
- Rosencwaig, A. (1980). Photoacoustics and Photoacoustic Spectroscopy. John Wiley and Sons, Inc.
- Sedlacek, A. and Lee, J. (2007). Photothermal interferometric aerosol absorption spectrometry. *Aerosol Sci. Technol.*, 41(12):1089–1101.
- Sedlacek, A.J. (2006). Real-time detection of ambient aerosols using photothermal interferometry: Folded Jamin interferometer. *Rev. Sci. Instrum.*, 77(6):064903.
- Sharma, N., Arnold, I.J., Moosmüller, H., Arnott, W.P., and Mazzoleni, C. (2013). Photoacoustic and nephelometric spectroscopy of aerosol optical properties with a supercontinuum light source. *Atmos. Meas. Tech.*, 6(12):3501–3513.
- Stier, P., Seinfeld, J.H., Kinne, S., and Boucher, O. (2007). Aerosol absorption and radiative forcing. *Atmos. Chem. Phys.*, 7(19):5237–5261.
- Strawa, A.W., Castaneda, R., Owano, T., Baer, D.S., and Paldus, B.A. (2003). The Measurement of Aerosol Optical Properties Using Continuous Wave Cavity Ring-Down Techniques. *J. Atmos. Ocean. Technol.*, 20(4):454–465.
- Wang, X., Heald, C.L., Liu, J., Weber, R.J., Campuzano-Jost, P., Jimenez, J.L., Schwarz, J.P., and Perring, A.E. (2018). Exploring the observational constraints on the simulation of brown carbon. *Atmos. Chem. Phys.*, 18(2):635–653.
- Ward, G.P., Hibbins, A.P., Sambles, J.R., and Smith, J.D. (2016). Acoustic transmission through compound subwavelength slit arrays. *Phys. Rev. B*, 94(2):1–7.
- Yelverton, T.L.B., Hays, M.D., Gullett, B.K., and Linak, W.P. (2014). Black Carbon Measurements of Flame-Generated Soot as Determined by Optical, Thermal-Optical, Direct Absorption, and Laser Incandescence Methods. *Environ. Eng. Sci.*, 31(4):209–215.
- Yu, Z., Assif, J., Magoon, G., Keabian, P., Brown, W., Rundgren, W., Peck, J., Miake-Lye, R., Liscinsky, D., and True, B. (2017). Differential photoacoustic spectroscopic (DPAS)-based technique for PM optical absorption measurements in the presence of light absorbing gaseous species. *Aerosol Sci. Technol.*, 51(12):1438–1447.

Zhang, X., Kim, H., Parworth, C.L., Young, D.E., Zhang, Q., Metcalf, A.R., and Cappa, C.D. (2016). Optical Properties of Wintertime Aerosols from Residential Wood Burning in Fresno, CA: Results from DISCOVER-AQ 2013. *Environ. Sci. Technol.*, 50(4):1681–1690.

Zuidema, P., Redemann, J., Haywood, J., Wood, R., Piketh, S., Hipondoka, M., and Formenti, P. (2016). Smoke and clouds above the southeast Atlantic: Upcoming field campaigns probe absorbing aerosol's impact on climate. *Bull. Am. Meteorol. Soc.*, 97(7):1131–1135.

Table 1. Geometric parameters for the two-resonator PA cell

Quantity	Description	Value
l_{res}	Length of resonators	11.0 cm
r_{res}	Radius of resonators	1.0 cm
d_{res}	Separation of the signal and reference resonator centres	2.2 cm
l_{buf}	Length of buffer volumes	5.5 cm ($l_{res}/2$)
h_{buf}	Height of buffer volumes	4.2 cm
w_{buf}	Width of buffer volumes	2.6 cm
r_{fil}	Fillet radius for corners of buffer volumes	0.8 cm
l_{win}	Length of window volumes	1.0 cm
r_{win}	Radius of window volumes	1.0 cm
θ_B	Brewster angle for UV fused silica at optical wavelength of 660 nm	55°

Table 2. Geometric parameters describing the optimised two-resonator PA cell.

Quantity	Value
l_{res}	9.2 cm
r_{res}	0.9 cm
d_{res}	2.1 cm
l_{buf}	6.4 cm ($0.7l_{res}$)
h_{buf}	4.1 cm
w_{buf}	2.6 cm
r_{fil}	1.2 cm ($0.9w_{buf}/2$)
l_{win}	1.0 cm
r_{win}	1.0 cm
θ_B	55°

Figure 1. (a) Example data for PAS microphone response, using the PA cell design of Lack et al. (2006), over time during airborne measurements aboard the UK research aircraft (FAAM BAe-146), including measurements for sampling ambient aerosol particles and for where the sample was passed through a HEPA filter (background). Measurements were made above the South East Atlantic Ocean during flight C043 of the CLARIFY-2017 field campaign based at Ascension Island (Zuidema et al. 2016). For comparison, we show the variation in pressure associated with changes in altitude over the range 0 – 7.5 km. The plot also shows the interpolated pressure-dependent background, using a quadratic polynomial to relate the background response to pressure. (b) The standard error in PAS-measured α_{abs} associated with uncertainty in the interpolated background microphone response.

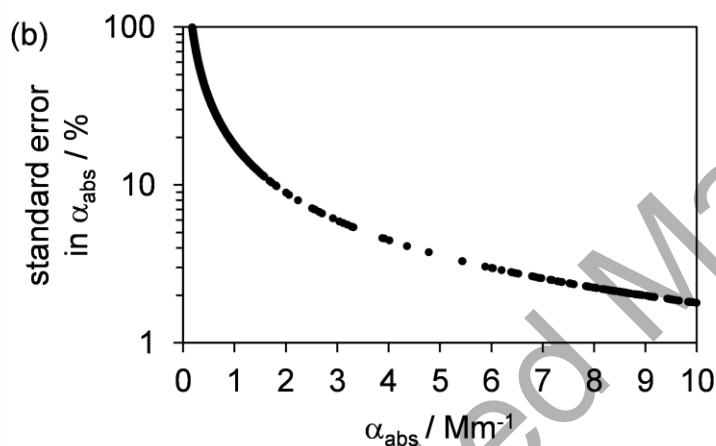
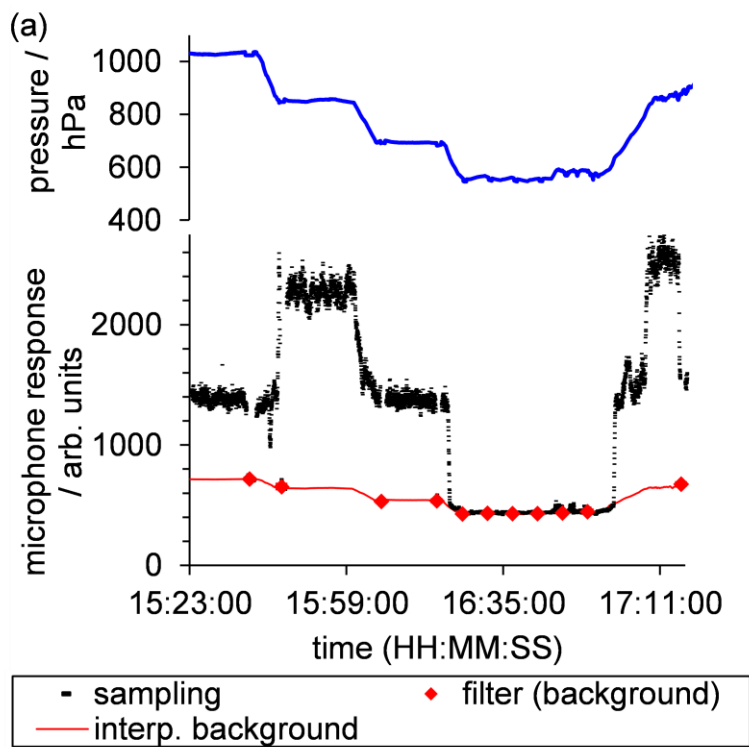


Figure 2. (a) The meshed geometry for the two-resonator cell with flat windows including two reflection symmetry planes; one parallel to the z - x plane through the centre of the cell (longitudinal mirror plane) and one parallel to the z - y plane (transverse mirror plane). (b) The meshed geometry for the Brewster window cell. (c) Labelled dimensions for the Brewster window cell, with perspectives along the longitudinal and transverse mirror planes. Table 1 provides values for these dimensions. (d) For the Brewster window cell, the highlighted volumes indicate regions where periodic *sample* or *window* heating were applied.

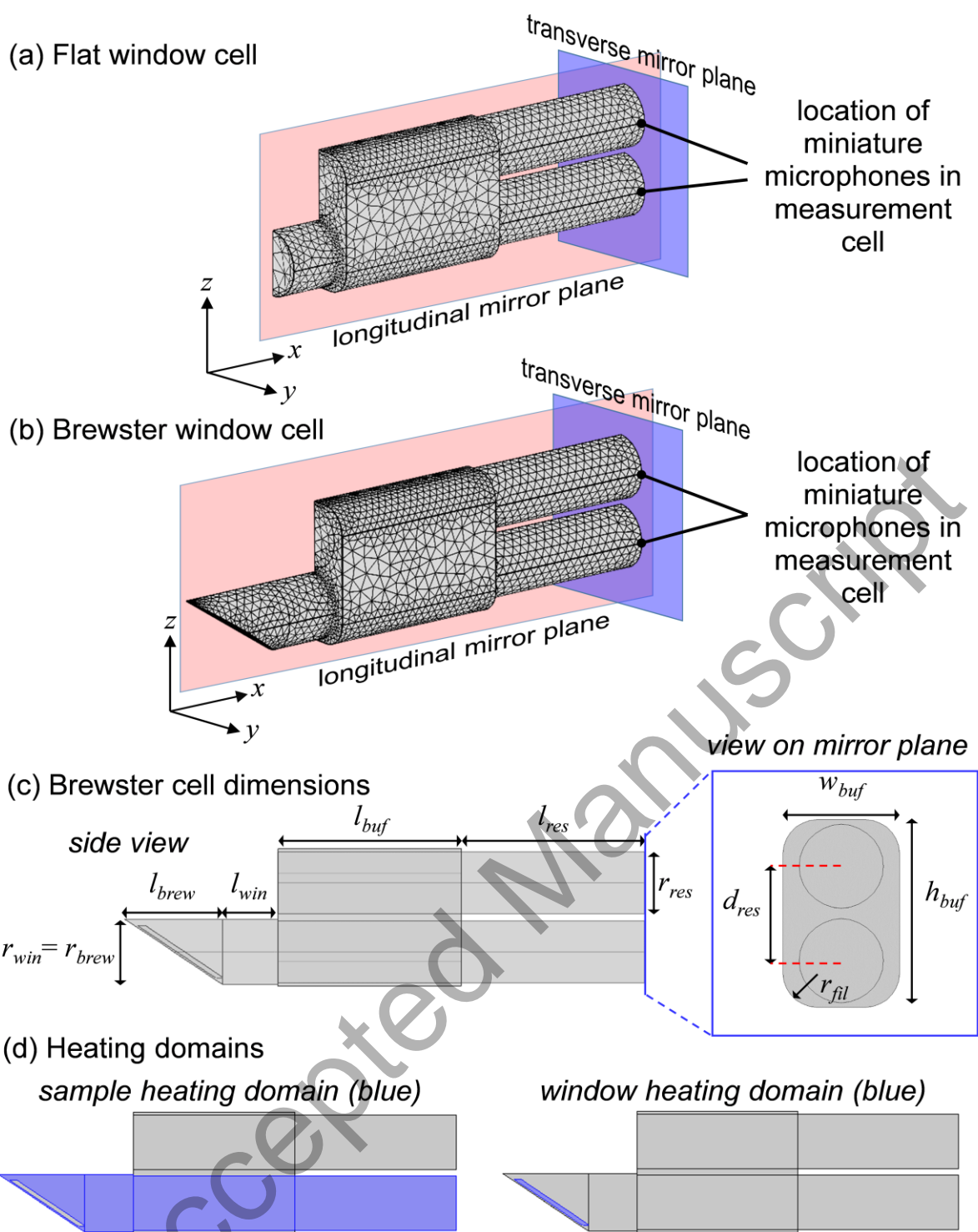


Figure 3. Comparison of the eigenmode pressure distributions for the two-resonator cell with either (a) flat windows, or (b) Brewster angled windows.

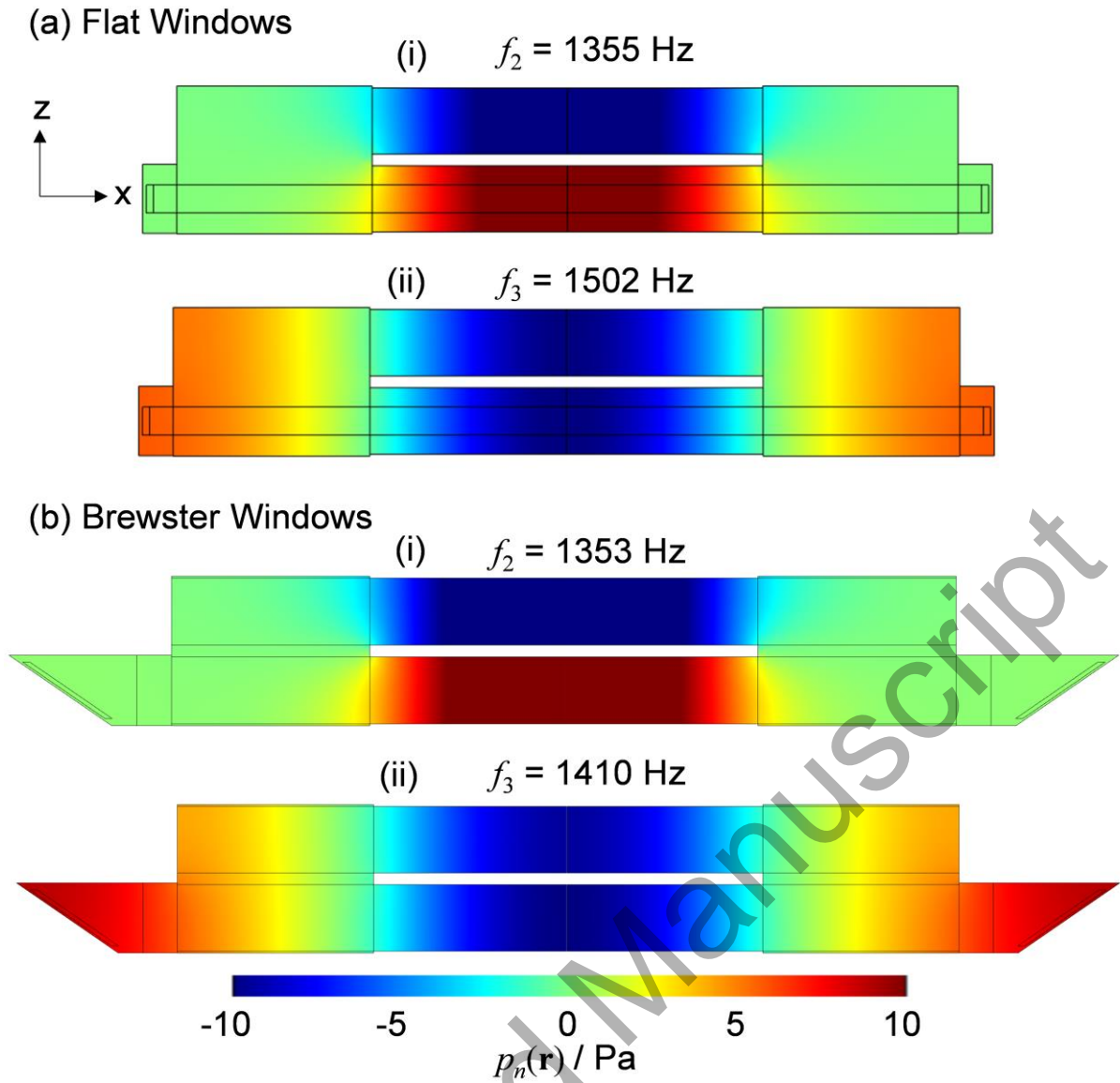


Figure 4. FEM predictions for the flat window cell of the frequency-dependent pressure responses $|p(\vec{r}_{M,low})|$, $|p(\vec{r}_{M,up})|$ and $|p(\vec{r}_{M,dif})|$. Simulations are shown for the cases of (a) sample heating ($\alpha_{sample} = 5 \text{ Mm}^{-1}$) and (b) window heating ($\alpha_{win} = 0.1653 \text{ m}^{-1}$). We compare the sample heating simulations to measured data using speaker excitation, with measurements representing the mean response over five PA spectrometers.

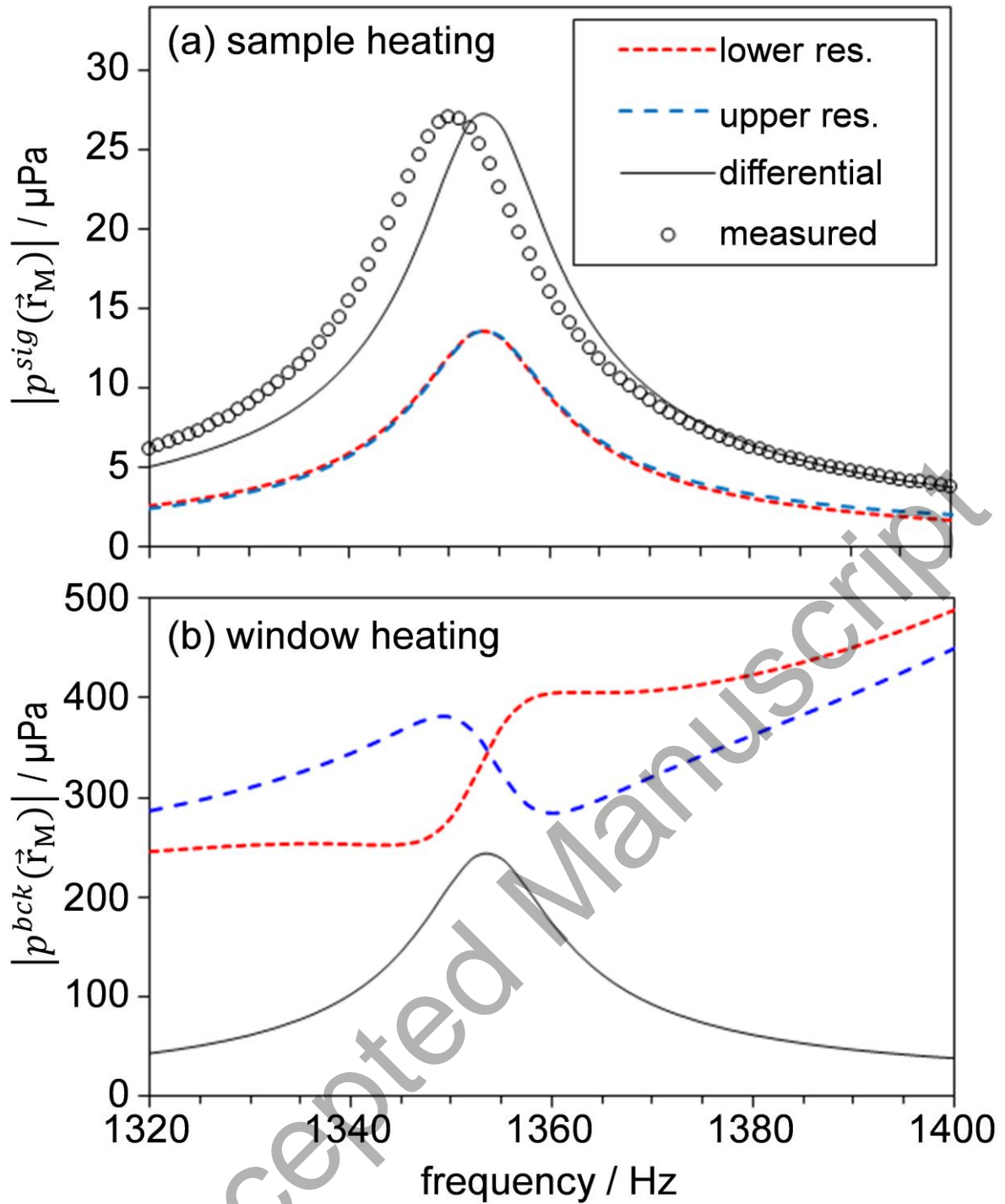


Figure 5. FEM predictions of microphone response for the Brewster window cell compared with measured data. (a) Simulations of $|p^{sig}(\vec{r}_M, \omega)|$ for the individual microphone and differential responses compared to measured differential operation data using speaker excitation. (b),(c),(d) Predictions of $|p^{bck}(\vec{r}_M, \omega)|$ (window heating) with the measured IA_{bck} for detection by the signal microphone, reference microphone and differential response, respectively. Measured data are shown for four separate PA spectrometers using 405 nm (two spectrometers), 514 nm or 658 nm laser excitation. The measured IA_{bck} has been normalised to scale from 0 to 1. The lines for the measured IA series are to guide the eye only.

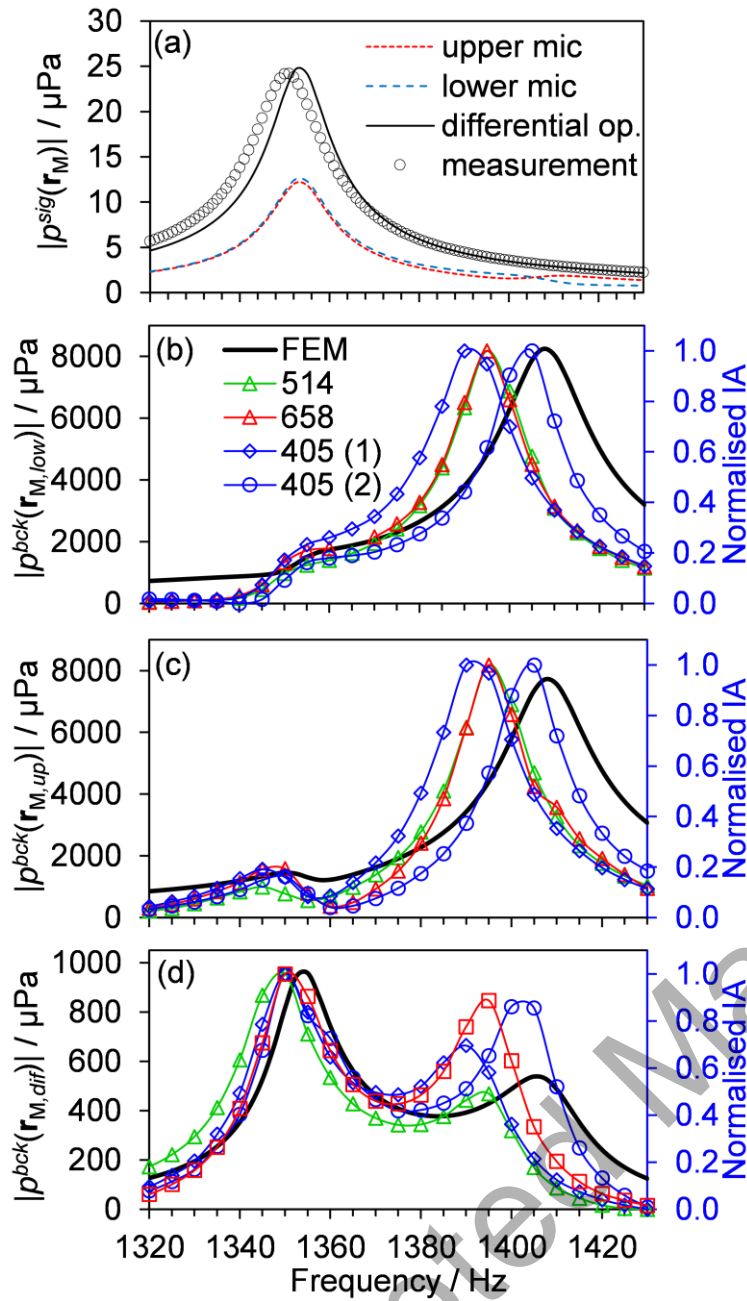


Figure 6. The eigenmode pressure distributions $p_n(\vec{r})$ for (a) the ring mode, and (b) the longitudinal mode with varying l_{buf} . The colour scale range has been expanded to emphasise important variations in $p_n(\vec{r})$ with changing l_{buf} . In particular, the variation in $p_n(\vec{r})$ within the window volumes for the ring mode and the eigenmode pressure in the two resonator pipes for the longitudinal mode is emphasised.

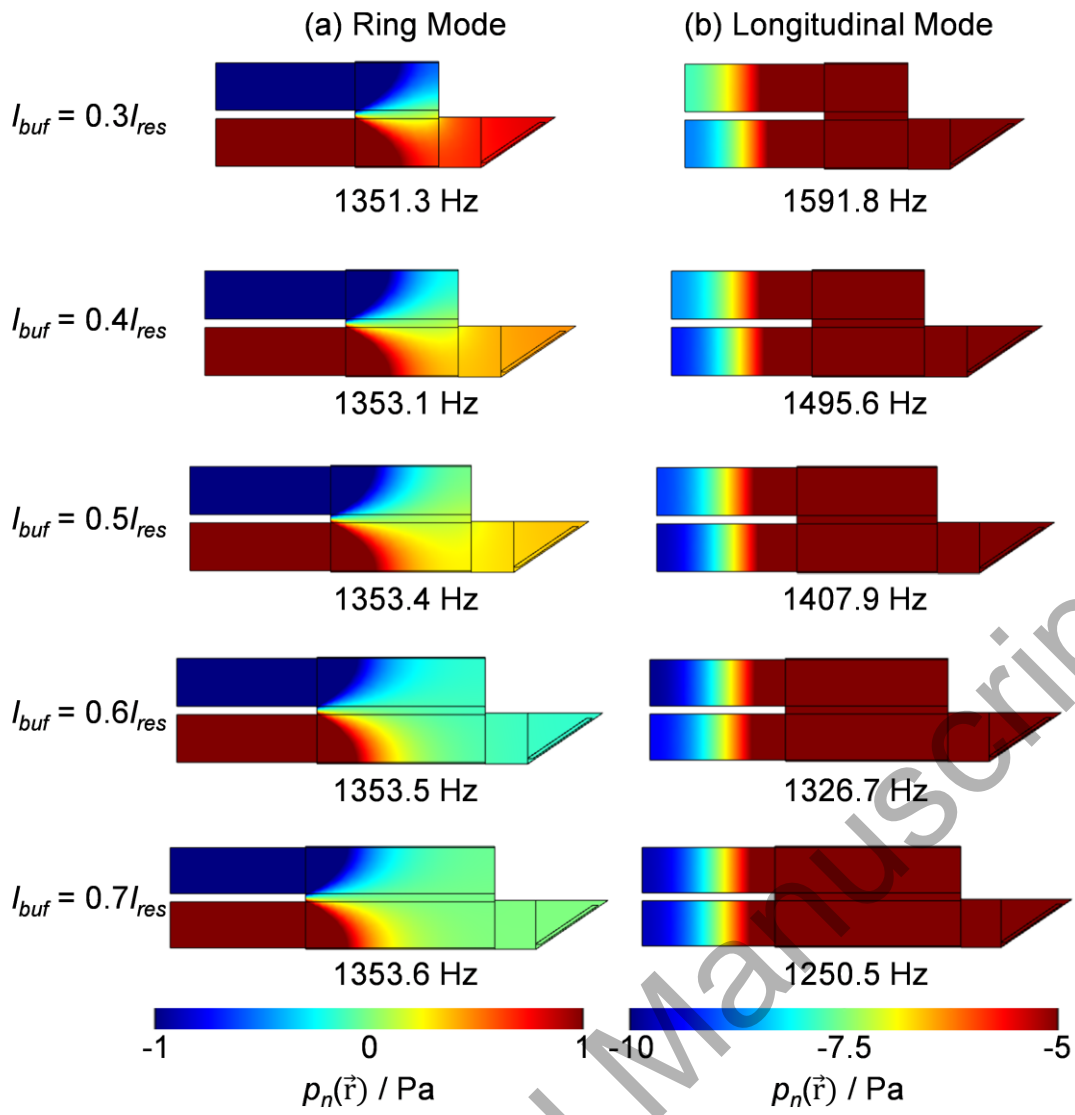


Figure 7. The FEM-predicted frequency dependence of (a) $|p^{sig}(\vec{r}_{M,dif})|$ and (b) $|p^{bck}(\vec{r}_{M,dif})|$ for values of l_{buf} in the range $0.1l_{res} - 0.7l_{res}$ in $0.1l_{res}$ intervals. The legend indicates the l_{buf}/l_{res} ratio for different series. (c) The variation in SBR with l_{buf} .

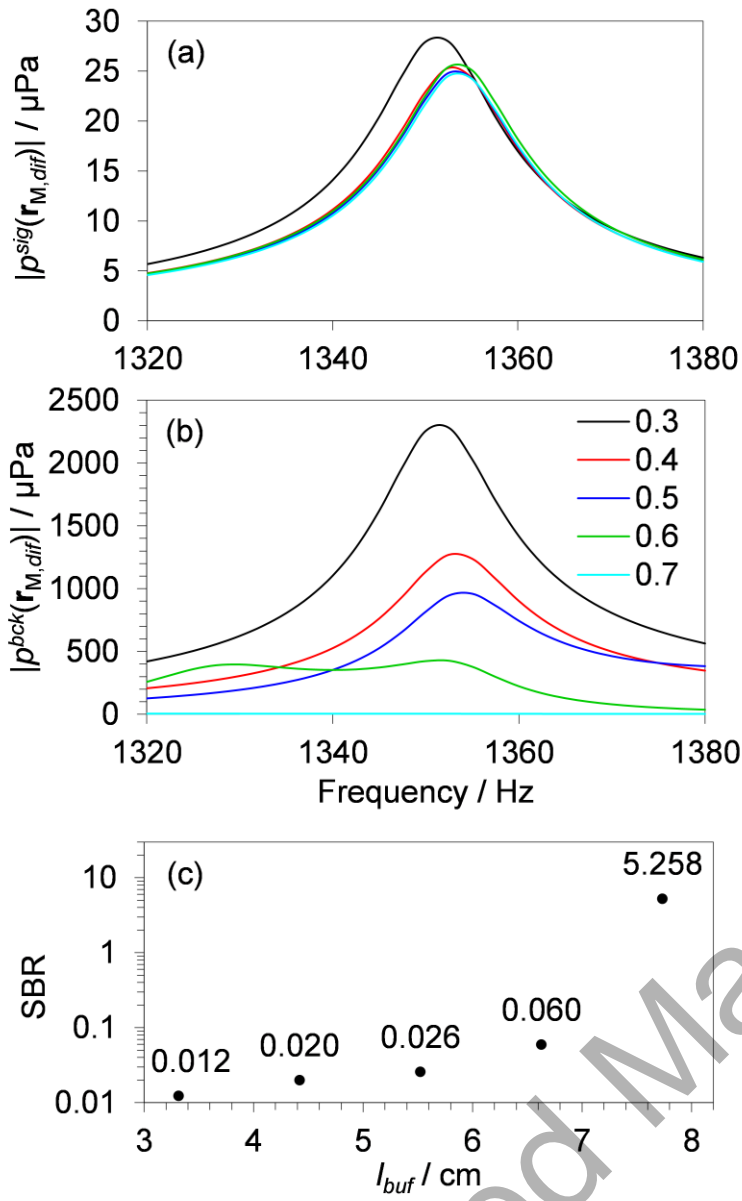


Figure 8. The variation in (a) $|p^{sig}(\vec{r}_{M,dif}, \omega_n)|$, (b) $|p^{bck}(\vec{r}_{M,dif}, \omega_n)|$, and (c) SBR with w_{buf} over the range 2.5 – 4.5 cm. Different data series are shown for the range of h_{buf} input to FEM simulations, from 4.5 cm to 6.0 cm in 0.5 cm steps. Lines are to guide the eye only.

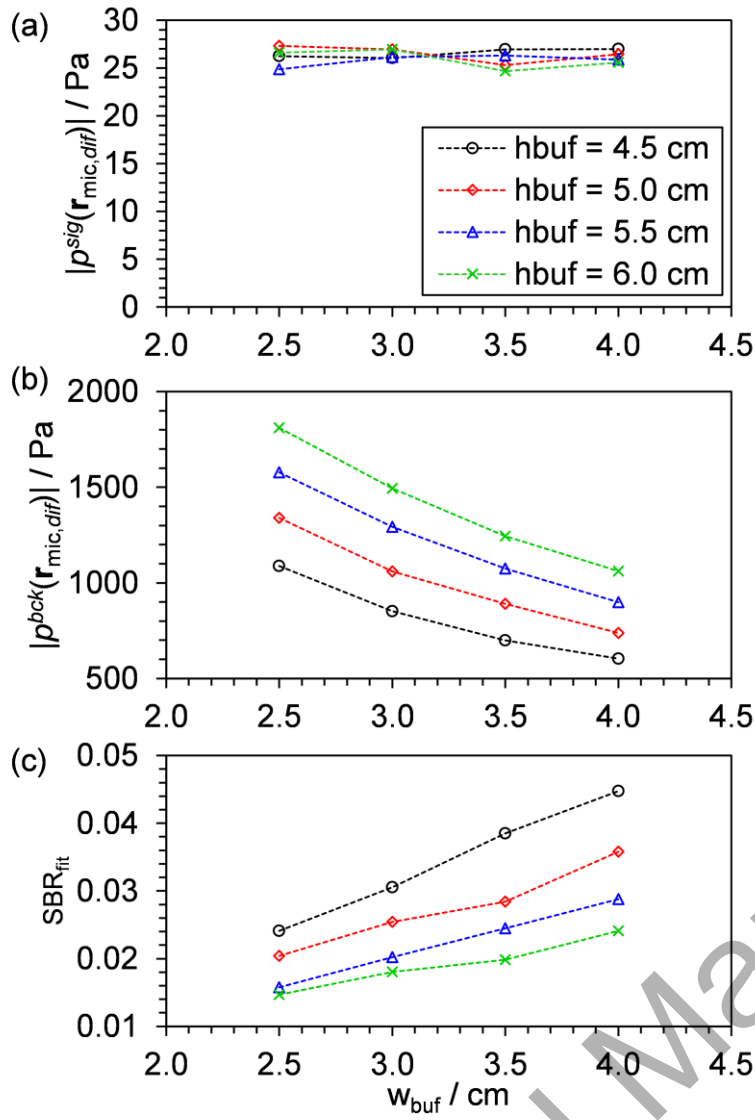


Figure 9. (a) The predicted SBR with variation in l_{buf}/l_{res} for the candidate two-resonator cell for which the total cell length is constrained to 22 cm, compared with the SBR variations presented in Figure 7. (b) Comparison of the predicted frequency-dependent differential amplified microphone responses for sample heating for the original (blue curve) and optimised (red curve) PA cells. (c) Same as (b) but for window heating excitation. The ring mode eigenfrequencies for the current (dashed blue line) and optimised (dashed red line) cells are indicated.

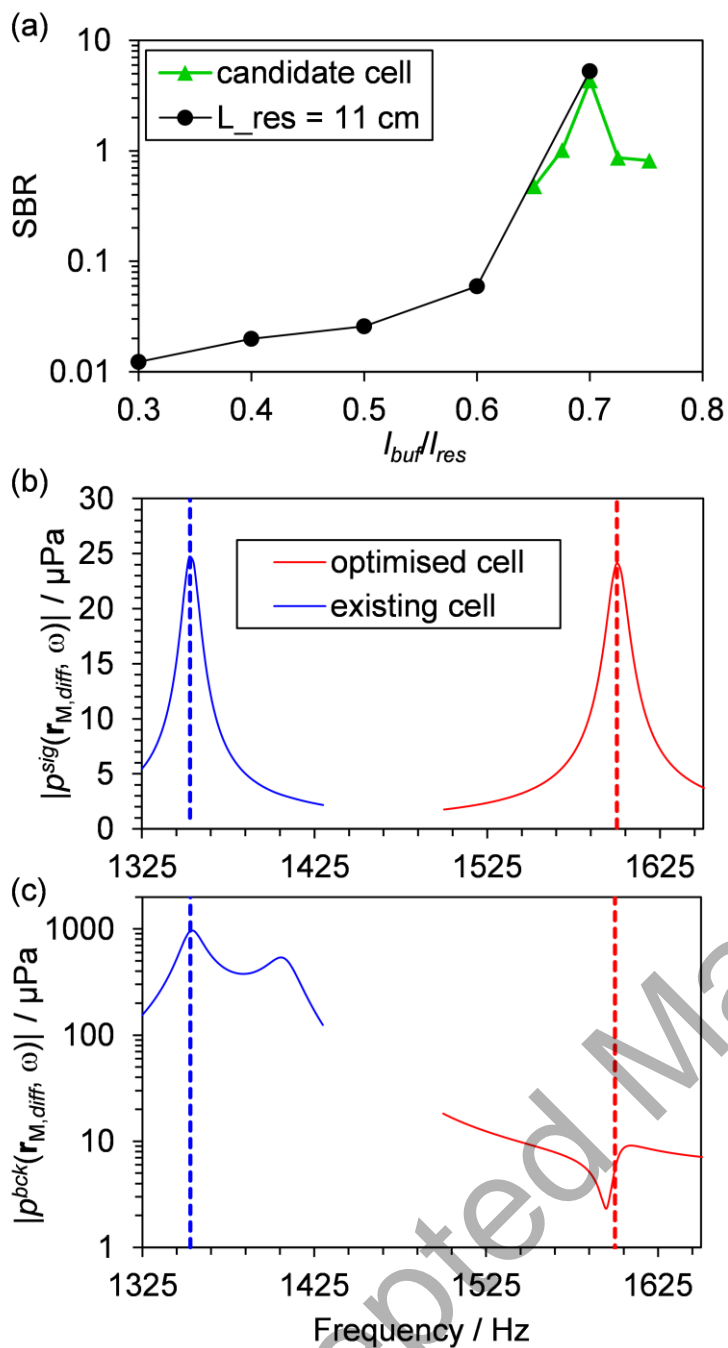


Figure 10. (a) For laser heating of the Brewster windows, the measured IA at the ring mode eigenfrequency for the original (old) and optimised (new) cells for laser wavelengths of 405 and 658 nm. The mean IA for ambient noise when the laser is off is also shown. (b) A time series in the measured IA for the optimised cell when the 658-nm laser is on or off. An indicative scale is shown on the right axis for absorption coefficient based on calibration of the cell using O_3 .

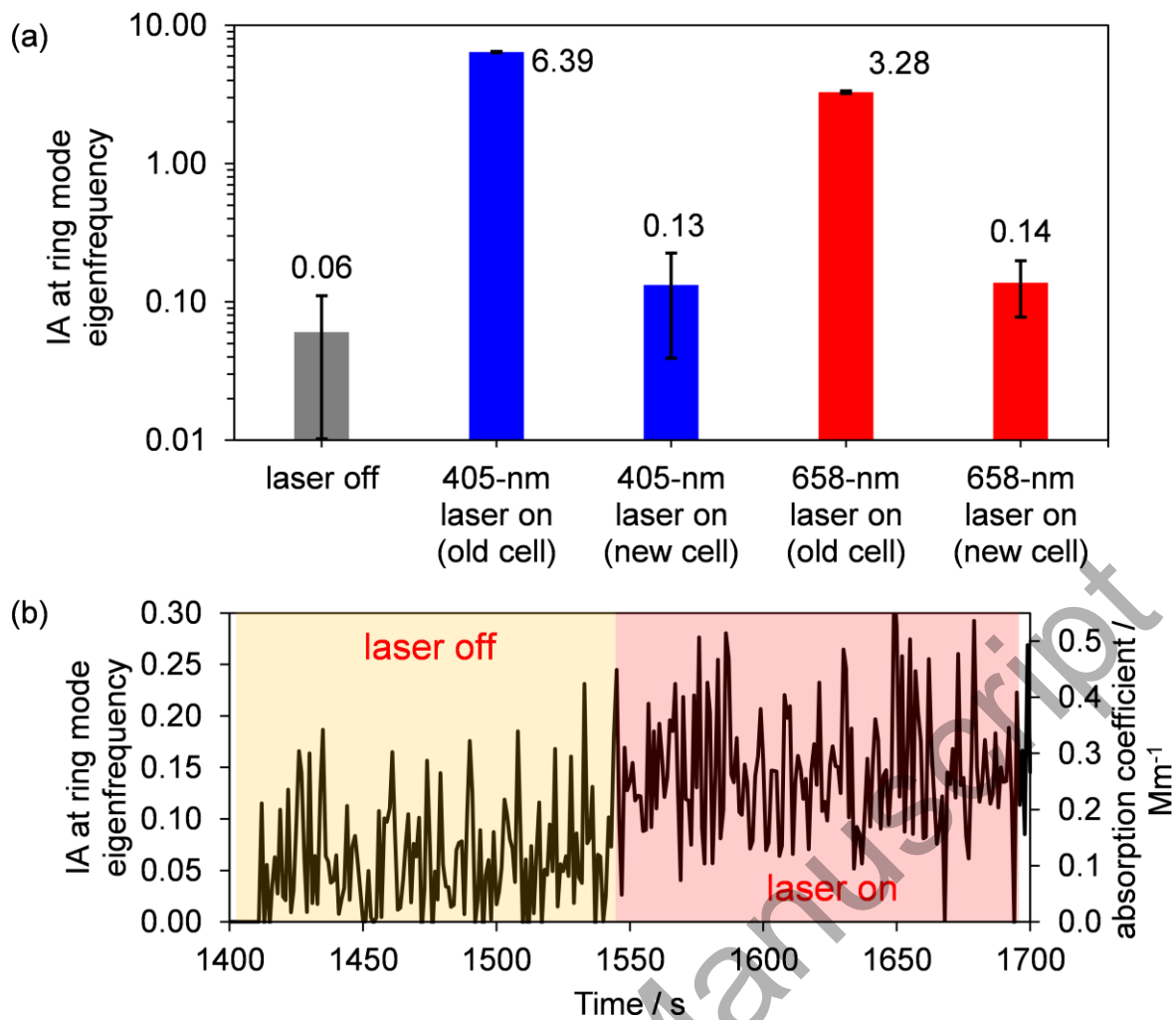
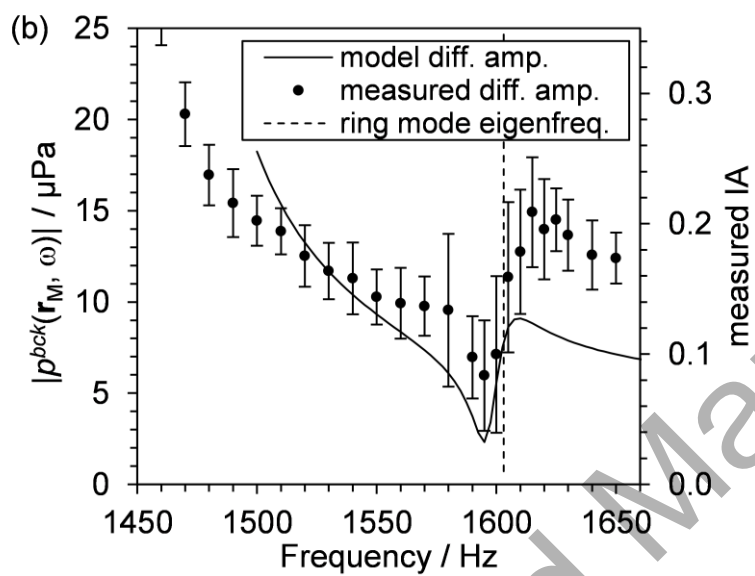
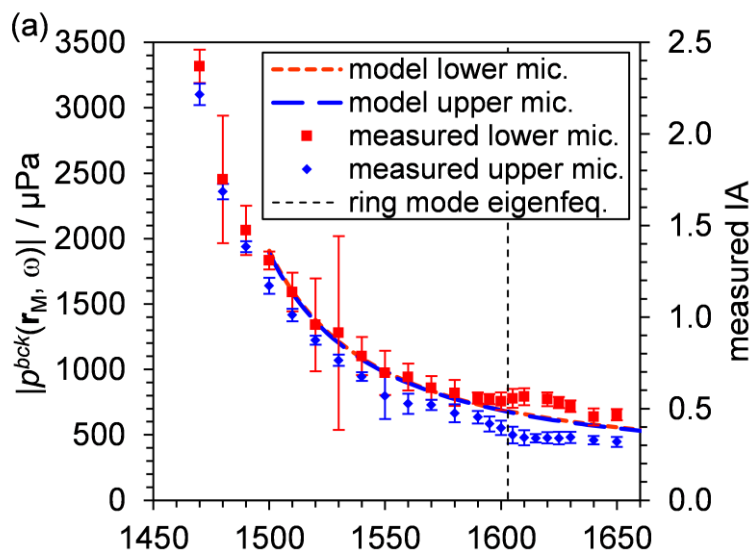


Figure 11. Comparison of FEM predictions of $|p^{bck}(\vec{r}_M, \omega)|$ with measurements of microphone response (IA_{bck}) for the optimised cell for (a) signal and reference microphone responses, and (b) differential amplifier response. Error bars in (a) and (b) indicate one standard deviation in the measured IA_{bck} for 30 s of measurements.



Accepted Manuscript